TESTING, ANALYSIS, AND MODEL VERIFICATION OF MINIATURE LINEAR PERMANENT MAGNET GENERATORS

by

Michael Ray Rippee

A thesis

submitted in partial fulfillment

of the requirements for the degree of

Master of Science in Mechanical Engineering

Boise State University

December 2012

BOISE STATE UNIVERSITY GRADUATE COLLEGE

DEFENSE COMMITTEE AND FINAL READING APPROVALS

of the thesis submitted by

Michael Ray Rippee

Thesis Title: Testing, Analysis, and Model Verification of Miniature Linear Permanent Magnet Generators

Date of Final Oral Examination: 19 October 2012

The following individuals read and discussed the thesis submitted by student Michael Ray Rippee, and they evaluated his presentation and response to questions during the final oral examination. They found that the student passed the final oral examination.

Donald Plumlee, Ph.D.	Chair, Supervisory Committee
John Chiasson, Ph.D.	Member, Supervisory Committee
John Gardner, Ph.D.	Member, Supervisory Committee

The final reading approval of the thesis was granted by Donald Plumlee, Ph.D., Chair, Supervisory Committee. The thesis was approved for the Graduate College by John R. Pelton, Ph.D., Dean of the Graduate College.

I would like to dedicate this to my loving wife, Jessica, and my parents Ted and Katie.

ABSTRACT

The military has become increasingly dependent on mobile electronic equipment to ensure success and safety of soldiers in remote locations. To operate the electronics, soldiers must carry batteries that can weigh up to 12kg (26.5lb). To decrease the load soldiers must carry, a backpack with an internal linear electric generator has been proposed to provide portable power for soldiers on foot. In designing a generator for this purpose, a simulation was developed to predict the power generation capacity of linear permanent magnet generators. This thesis presents work done to experimentally verify the theoretical simulation with a desired accuracy of 20%. An experimental power-testing apparatus was developed and used to test four geometries of generators. After initial comparisons gave unacceptable error, the magnetic field prediction was adjusted to provide better accuracy. After the adjustment, the model was shown to predict average power generation of the four generators within 11% accuracy. The simulation was then used to predict an optimal linear generator consisting of stator coils made of 32awg wire with 267 windings of wire.

TABLE OF CONTENTS

LIST OF TABLES

LIST OF FIGURES

LIST OF SYMBOLS

B_g Flux density at distance radially outward from magnet surface (T)

$\hat{B}_g$ Magnetic flux density at surface of magnet (T)

B_r Remnant flux density of magnet (T)

cw Width of stator coil windings (m)

ch Height of stator coil windings (m)

D Duty cycle (%)

D_o Initial Duty cycle (%)

F Inductive coupling force due to segment of wire (N)

F_{coil} Inductive coupling force due to entire stator (N)

f Frequency (Hz)

f_o Initial Frequency (Hz)

gap Distance between surface of magnet and inner radius of stator (m)

I Current (A)

J Current density ($\frac{Amp}{m^2}$)

K_I Integral controller constant

K_P Proportional controller constant

l_g Length of Air gap (m)

L_p Path length of wire in stator (m)

P Electric Power (W)

R Resistance (Ω)

r Distance Away From Magnet (m)

R_i Inner radius of stator (m)

R_m Radius of Magnet (m)

R_o Outer radius of stator (m)

R_{sis} Internal resistance of stator windings (Ω)

R_{tot} Total resistance of circuit (Ω)

V Voltage (V)

v Linear Velocity of Translator($\frac{m}{s}$)

vol Volume containing stator coils (m^3)

w_m Width of Magnet (m)

w_s Width of Steel Spacer (m)

μ_r Relative Permeability

CHAPTER 1

INTRODUCTION

1.1 Justification for Portable Power

As technology has developed, people have grown accustomed to the advantages of electronic devices to improve their ability to perform certain tasks. The technology development within the military has enabled soldiers to perform missions more safely, more efficiently, and more reliably. Some examples of equipment that soldiers could have to carry are: on-board computer, radio, global positioning system, thermal imaging equipment, laser range finder, and video sights on weapons [1]. The main drawback of having such sophisticated equipment is that it requires a power source to operate, and many missions where the equipment is used are in remote locations where no power source is available.

Figure 1.1 displays an experimental equipment system that was developed for soldiers to use when deployed in the field. The soldier is carrying a thermal weapon sight and a daylight video sight on his weapon. He has a heads-up-display (HUD), and a mouse to operate an on-board computer, which is not shown in Figure 1.1. He has a COM-M/AV module and a microphone/speaker for communications. In addition to that extra equipment, he is also carrying a large battery to power those systems.

Most electronic devices contain batteries to provide power for operation. Batteries are a great method for energy storage on a small, temporary scale. When no power source is

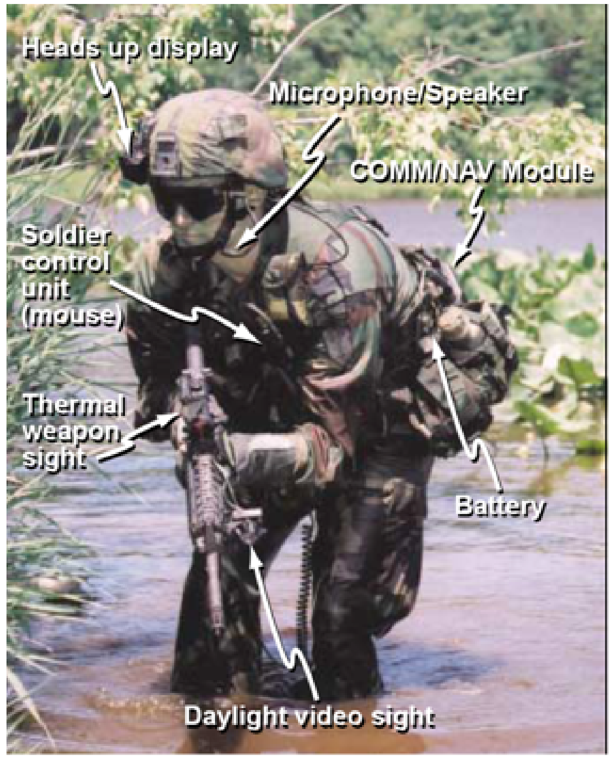

Figure 1.1: Example of Technology System Being Developed for Deployed Soldiers [1]

available to recharge the batteries, replacements must be available to enable extended use of the equipment. Patel-Predd found that on a three day mission, a soldier must carry as much as $12kg$ ($26.5lb$) of batteries to power all of the equipment [2]. For soldiers on foot, $12kg$ is a substantial burden to add to the other necessary supplies the mission might require. Quesada et al. found that the the gait of a loaded subject changes when marching under heavy loads, which could increase the risk of injury [3]. To minimize the load that soldiers have to carry, a goal of 50% reduction in weight is put in place. Based on the maximum battery load of $12kg$, the desired weight of a portable power device should be $6kg$ or less.

Recreational hikers are similarly affected by the prominence of portable electronics and a lack of power sources. Electronics usage is increasing and hikers are having to carry larger loads of batteries in order to power all of their equipment. They use devices such as two-way radios, cellular telephones, digital cameras, GPS devices, flash lights, and various other equipment. Generally, they are in remote locations where no power source is available, and most consumer devices have limited battery life. To extend use of equipment, extra batteries must be purchased and carried, adding substantial weight and cost.

1.2 Defining the Portable Power Needs

In order to develop a solution for portable power, it is important to define the amount needed. Energy use is a wide-ranging subject based on the intended use. It is difficult to meet all energy needs with one source of generated energy. Due to the portability required to meet the needs of the ground soldier, the amount of energy needed is an important constraint to consider. A successful system will have the capacity to provide energy that the soldier needs without excess. To ensure a system will meet the energy needs without overburdening, it needs to be designed for a precise generation capacity. To get the proper capacity, the current energy use of personal military systems was analysed to determine the power needs of soldiers.

Table 1.1 displays the amount of power required for various equipment used by a soldier in the field. The table is composed of two columns. The left column lists the individual electronic devices in the land warrior system, and the right column indicates the power used by each piece of equipment. There are three individual categories within the system, each of which has a subtotal power usage displayed, in addition to the total power of the system shown in the final row. It can be seen that the entire land warrior system requires a total of $56.7W$ to run all of the on-board system, however it is not likely that all systems would be running at the same time. For example, the receive and transmit functions of the soldier radio and squad radio are not able to be accessed at at the same time. Assuming a typical usage pattern, there is an average power consumption of approximately $4W$.

Table 1.1: Power consumption of individual electronic devices that make up the land warrior system, a personal combat system designed for soldiers [4]

	Functional Operating Power (W)
Computer/Radio Subsystem	
Computer	14.800
Hand-Held Flat Panel Display	6.400
Soldier Radio	
Receive	1.400
Transmit	6.000
Squad Radio	
Receive	2.000
Transmit	12.000
Global Positioning System	1.500
Video Capture	1.000
Subtotal	**45.100**
Integrated Helmet and Sight Subsystem(IHAS)	
Laser Detectors	0.600
Helmet Mounted Display	4.900
Imager	0.100
Subtotal	**5.600**
Weapon Subsystem	
Laser Range finder	0.050
Laser Aiming Light	0.075
Digital Compass	0.350
Thermal Weapon Sight	5.525
Subtotal	**6.000**
TOTAL	**56.7**

Figure 1.2 is a graph showing the power requirements of various, personal, electronic equipment. The graph displays stored energy on the horizontal axis in units of Wh, required power on the vertical axis in units of W, and run time on the light gray diagonal axis in units of min and h. Markers numbered 2, 3, and 4 indicate the needed performance to power a cell phone, 4G cell phone, and minimal wearable computer, respectively. These are the types of device that are going to be carried by soldiers and hikers, and therefore these are the devices that are being focused on. All of these devices have a desired run

time of between $1h$ and $10h$ and a power requirement of $1W$ to $10W$. The maximum stored energy required in this range is approximately $100Wh$.

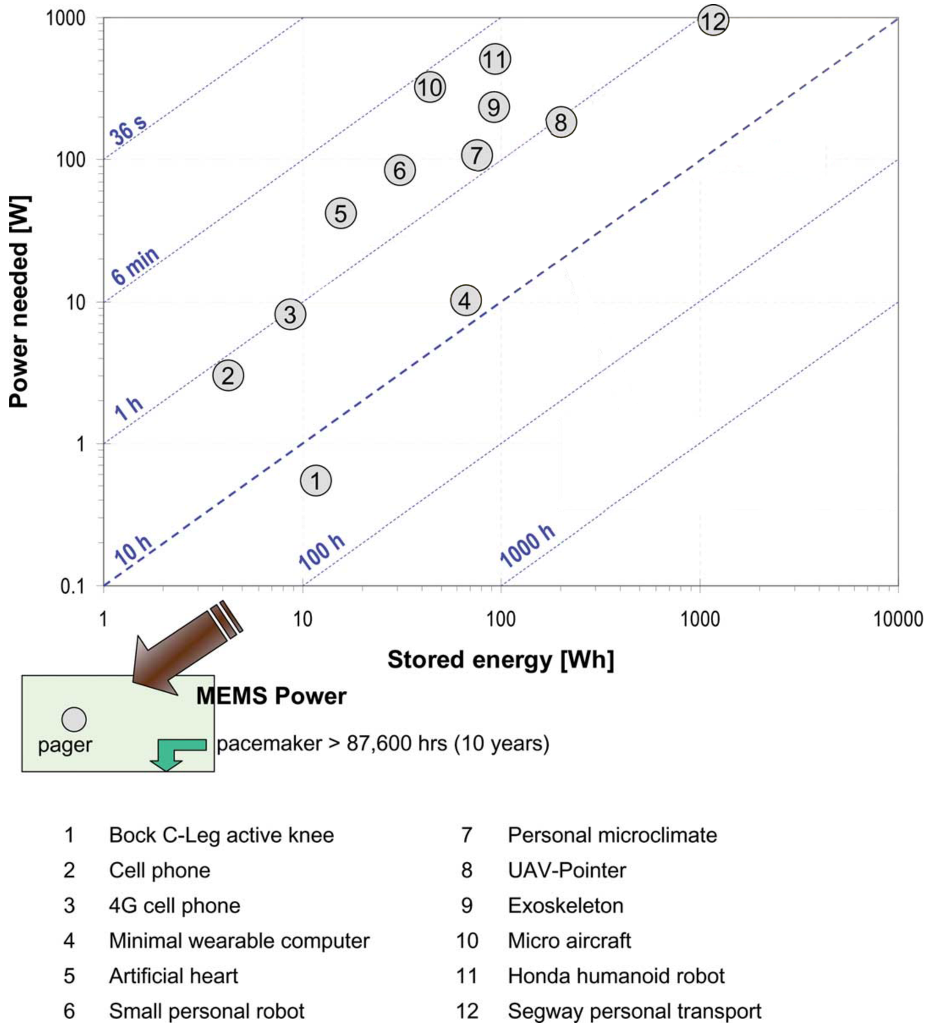

Figure 1.2: Power needed(W) vs. Stored energy(Wh) of various portable electronic equipment [5]

Based on Figure 1.2 and Table 1.2 it can be seen that a portable power source that could produce $1W$ to $10W$ of continuous, dependable electric power could displace most of the batteries that are required to run equipment used by hikers and soldiers in the field. Various portable power generation devices exist that are meant to generate power in the range of less than one Watt up to thousands of Watts. A Ragone plot was used to compare various common power sources. A Ragone plot compares energy density in $(\frac{Wh}{kg})$ to power density in ($\frac{W}{kg}$). The energy density is a measure of how much energy can be produced, or stored, per unit mass of the device. The power density is a measure of how much power can be produced or stored per unit mass of a device. By comparing these two values, it gives an idea of how much energy can be generated and how fast it can be delivered. In order to provide power to operate or charge small electronics, it is desirable to have large amounts of energy density with relatively small power density in order to produce small amounts of power for long periods of time. Figure 1.3 displays a Ragone plot of power sources considered by Dunn-Rankin et al. [5].

In Figure 1.3, the horizontal axis represents the energy density in ($\frac{Wh}{kg}$) and the power density is on the vertical axis in ($\frac{W}{kg}$). Both axis are displayed in a log scale to allow a large range of sources to be shown clearly. A rectangular area has been marked, indicating the desired region for a device to be located if it is to be used as a portable energy generation device. The desired region spans from $2\frac{W}{kg} - 200\frac{W}{kg}$ of specific power and from $2\frac{Wh}{kg} - 200\frac{Wh}{kg}$ of stored specific energy. These values are based on the desired ranges of mass and power from Figure 1.2 and Table 1.1.

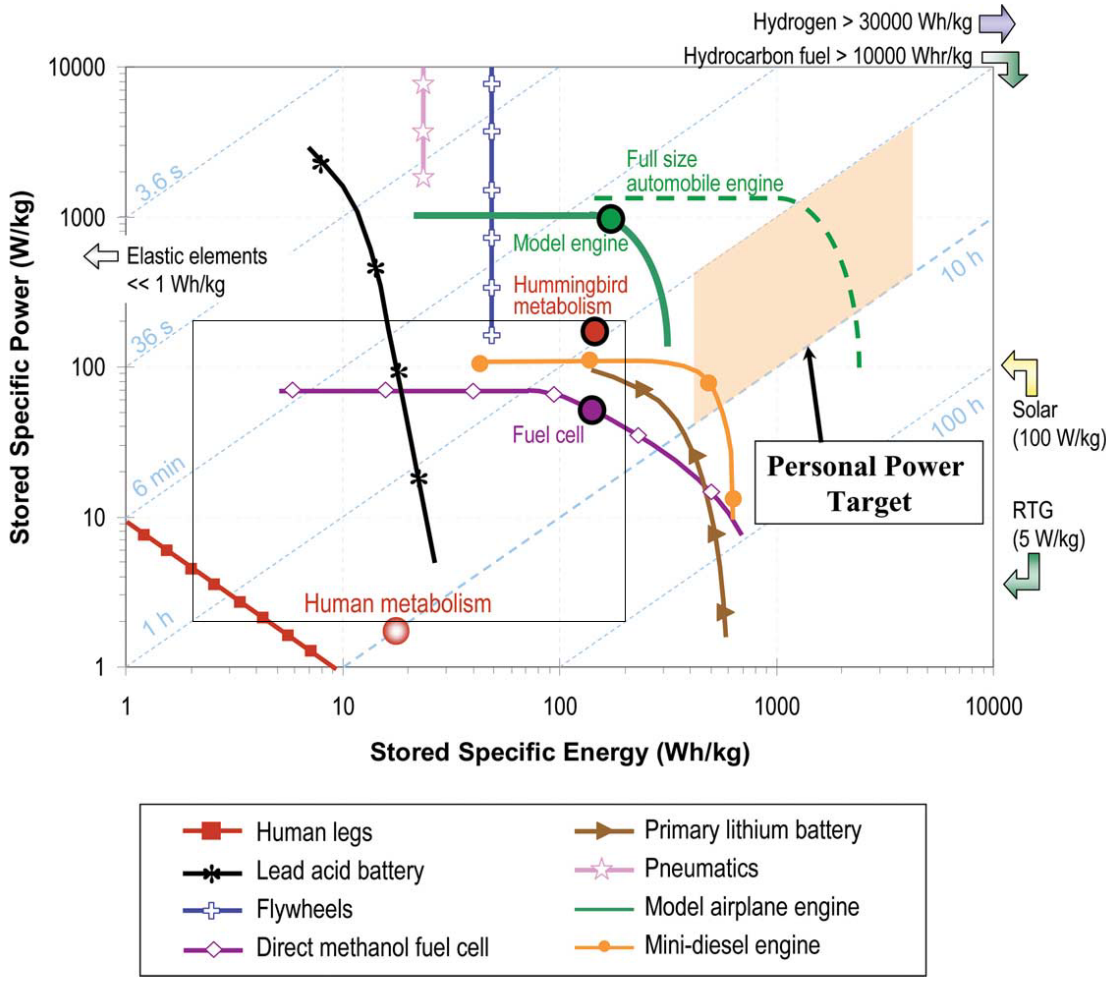

Figure 1.3: Ragone plot comparing energy density and power density of small scale power sources [5]

Of particular interest in Figure 1.3 is the red line with square point markers, indicating human legs. Energy scavenging from human motion is an option for power generation that will be explored further in this thesis. The human legs curve falls within the low end of the desired spectrum of a portable power device. Other sources that fall within the desired range are batteries, methanol fuel cell, and mini-diesel engine. Both the fuel cell and mini-diesel engine require an external fuel source, which adds extra weight and possible safety hazards.

A second Ragone plot, shown in Figure 1.4, shows a comparison of energy density and power density of thermoelectric, photovoltaic, and piezoelectric devices. The horizontal axis displays the power density in ($\frac{W}{kg}$), the left vertical axis shows energy density in ($\frac{J}{kg}$), and the right vertical axis shows energy density in ($\frac{Wh}{kg}$). Thermoelectric and photovoltaic devices have similar power and energy densities, both falling in a range of $10^0\frac{W}{kg} - 10^1\frac{W}{kg}$ power density and $10^0\frac{Wh}{kg} - 10^3\frac{Wh}{kg}$ energy density. The power density of the piezoelectric devices is in the range of $10^{-2}\frac{W}{kg}$ and the energy density is in the $10^{-3}\frac{Wh}{kg}$ range. These three devices are all energy scavenging devices that are discussed as possible portable power sources.

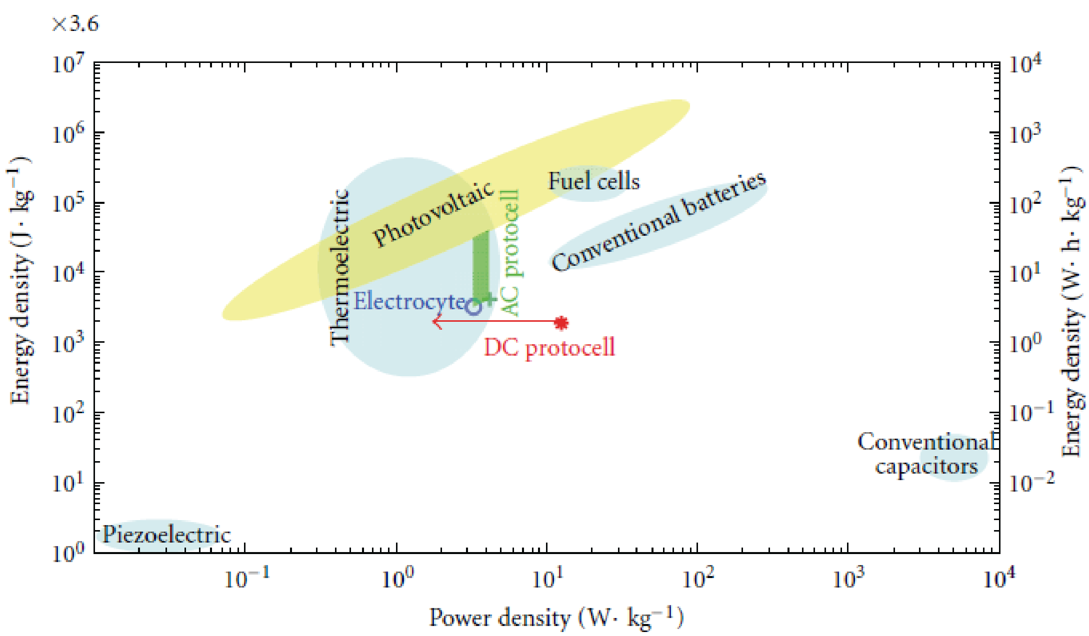

Figure 1.4: Ragone plot comparing energy density and power density of thermoelectric, photovoltaic, piezoelectric, and chemical energy storage devices [6]

All of the devices discussed from Figures 1.3 and 1.4 are energy scavenging devices. They are ideal for portable power needs because they do not require an external fuel source. Section 1.3 goes into further discussion to examine what an energy scavenging device is, and how a number of prospective devices will meet the power needs of soldiers in remote locations.

1.3 Introduction to Energy Scavenging Devices

To avoid the need to pack fuel for a power generator, energy scavenging devices have been considered as a possible portable power source. Energy scavenging devices make use of surrounding environmental sources such as solar, wind, thermal, hydro, and kinetic energy. Many such devices exist that were designed for applications such as providing clean renewable power, providing power where transmission lines are expensive or unavailable, and recuperating wasted energy to be used for meaningful work.

A number of devices that have the proper power and energy density to fill the need of portable power are shown in Figures 1.3 and 1.4. Generators that require a separate source of fuel would be at a disadvantage due to weight constraints and possible hazards of certain fuel sources. Power sources that require a fuel source would require the soldier to carry the fuel, which adds excess mass to their load, and many fuel sources pose a health hazard from exposure. Some of the devices that fall under this category are the PEM fuel cell, Direct Methanol fuel cell, and mini-diesel engine. These devices have desirable power density and specific stored energy ratings, but are not practical to take into remote locations

Photovoltaic solar panels are a popular and widely used form of energy scavenging device. They have been in use for decades and have been proven as a good source of clean renewable energy. In the last decade, miniature panels have been developed for use as personal power to charge electronic devices such as cell phones, radios, digital cameras, and various other small electronic devices. As seen in Figure 1.4, photovoltaic cells fall well within the range of power density that is desired for this application. A large drawback to photovoltaic cells is the need for a consistent source of sunlight to operate. Photovoltaic cells lose efficiency in many terrains, including areas that receive minimal sunlight such as areas with heavy trees, and in canyons where sunlight only penetrates for a short amount of the day. They require a direct sunlight to operate, thus they must be focused directly on the sun inhibiting them from being used effectively unless they are left stationary.

Another form of energy scavenging uses piezoelectric devices. These are devices that generate electricity when deformed. These devices can be small, lightweight, and produce large peaks of voltage. There have been multiple designs, using piezoelectric technology, with the purpose of providing personal electrical power generation to a person by scavenging energy out of a persons movement while they walk. Feenstra et al. [7] replaced the buckle on a backpack strap with a piezoelectric actuator stack, so that as a person walks with the backpack, their motion would deform the stack and generate electricity. Figure 1.5 displays the experimental set-up of Feenstra et al. The piezoelectric stack can be seen in the inset image in Figure 1.5. This stack was put under a load that fluctuated between approximately $55N$ and $100N$ and produced a peak power of approximately $1.5mW$ at a peak of $4V$.

Figure 1.5: Backpack with a piezoelectric actuator stack in place of bottom strap buckle [7]

Shenck et al. designed a scavenging piezoelectric device that mounts inside the shoe either near the heel or the ball of the foot [8]. The shoe mounted piezoelectric device produces power as a person transfers their load to the foot. The force of the persons load is transmitted from the foot onto the piezoelectric plate, causing deformation of the plate, which causes a voltage potential. Figure 1.6 shows a pair of shoes with a device installed. A cord can be seen coming out of the back of the shoe and going into the controller mounted on the outside of the shoe. This device generated $8.4mW$ of power at a peak of $44V$ [8].

Figure 1.6: Shoe with piezoelectric generation device installed in the heel [8]

Both Shenck et al. and Feenstra et al. did studies focused on using piezoelectric devices for energy harvesting. Both studies provide results showing the power generation of piezoelectric devices is on the order of milliwatts. As stated in Section 1.2, the range of generation desired for this study is from $1W - 10W$, indicating that piezoelectric generators will not provide enough power to charge personal electronics.

Another approach to energy scavenging is to use a standard electromagnetic generator to convert mechanical energy into electrical energy via a changing magnetic flux in coils of wire. A application of this is in auto-mobile alternators, which harness the rotation engine crank shaft to generate electrical power to charge the auto-mobile battery.

Rome et al. [9] devised an energy scavenging system using an electromagnetic generator built into a backpack frame to harvest energy from the movement of a person wearing the device. Figure 1.7 displays the design for this backpack. The pack body is mounted to two vertical slides that are attached to a harness worn by a person. The pack is suspended from four springs that attach to a solid frame on the harness. By suspending the load of the pack, it is allowed to oscillate vertically on the harness as a person moves. The pack has a linear rack gear attached to the pack mounting plate. An electric generator is mounted to the harness frame, with a pinion gear attached to the generator shaft. The rack and pinion mesh to convert linear oscillations of the pack to rotary motion of the generator shaft. As the pack oscillates, the rack gear oscillates as well, causing the pinion gear to rotate the shaft of the generator.

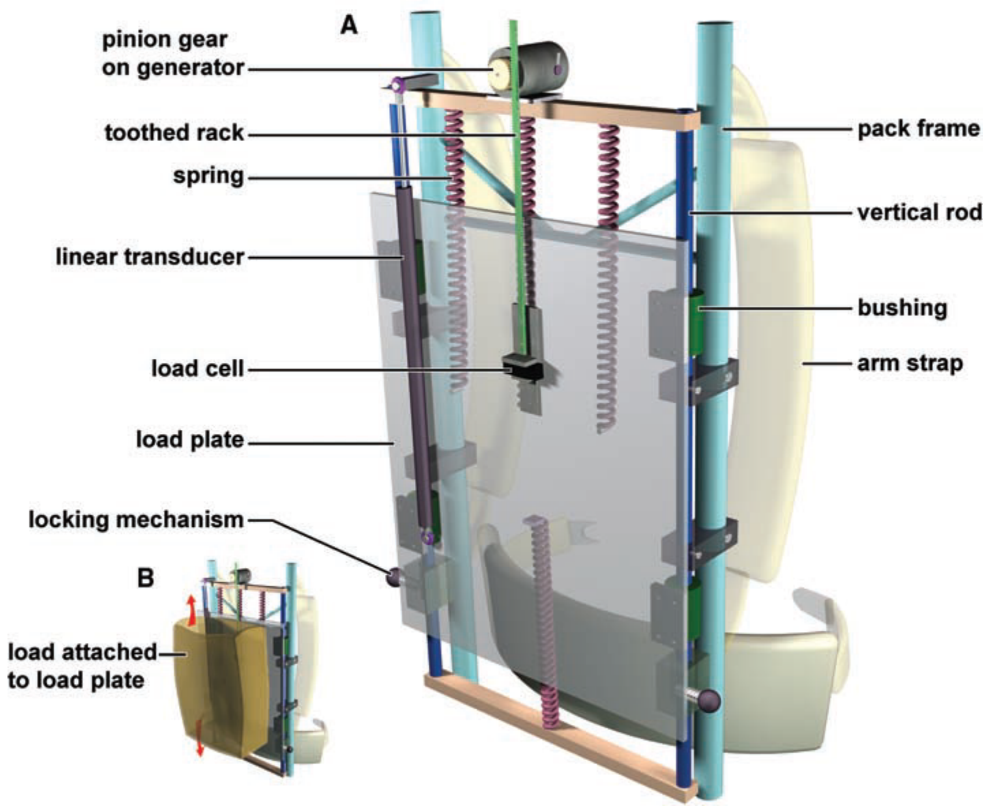

Figure 1.7: Backpack mounted on vertical slides with a rotary electric generator [9]

The backpack system designed by Rome et al. was generating $7.4W$ of peak power at loads of $20kg - 38kg$. The experimental apparatus weighed $5.6kg$ and Rome et al. has hopes of reducing the apparatus weight to $1kg - 1.5kg$ in future designs [9]. Of the scavenging devices reviewed, this design is the only one that could produce enough power to achieve the desired range of $1W - 10W$. The original design of Rome et al. is near the maximum desired weight limit of $6kg$ as stated in Section 1.1. The system is integrated into the framework of the backpack, therefore the size of the apparatus is not a constraint as it will not have to be contained in the limited space of the backpack storage area.

The design of Rome et al. is very promising and has shown that it has the capability to generate the required power to operate multiple devices at the same time. There are some concerns related to the durability of the system of Rome et al. in military applications. The requirement of the rack and pinion to mesh properly could create an inability to function when subjected to physical stress. If the frame were placed under stress that caused the generator shaft or rack to bend, the gears would cease to mesh properly. Fragility of the system is a large concern when designing for military applications, because military equipment will be subjected to hostile environments and be required to function properly with abuse.

To eliminate the fragility of the gearing system within the design of Rome et al., linear permanent magnet generators were researched as a possible replacement for the rotary generator. This would eliminate the need to convert linear motion of the backpack to the rotary motion of the generator shaft. It could be directly driven by the movement of the backpack frame, eliminating the need for meshing gears. Elimination of the gear system would also decrease inefficiencies due to friction in the gears.

1.4 Linear Permanent Magnet Inductive Generator

The system Rome et al. designed meets the criteria specified in Sections 1.1 and 1.2 for power and size requirements. Unfortunately, there are some concerns with inefficiencies and fragility of the rack and pinion system. In order to use a rotary generator, the motion has to be converted from a linear translational to a rotational movement. By using a linear permanent magnet generator, the movement of the backpack could be converted directly to electrical energy without first going through a gear system.

Linear permanent magnet generators have been used to convert ocean wave energy into electrical energy [10–12]. Figure 1.8 shows an example of a linear generator used to convert wave momentum to electrical energy [13]. The system uses a buoy located on the surface of the water that rises and falls with the waves to provide movement to the generator. A rope connects the buoy to an actuator, commonly called a translator, that holds a stack of permanent magnets as shown in the picture. The stator consists of sections of wound wire that surround the stack of magnets. As the actuator oscillates within the stator, the changing magnetic field induces a current within the coils of wire.

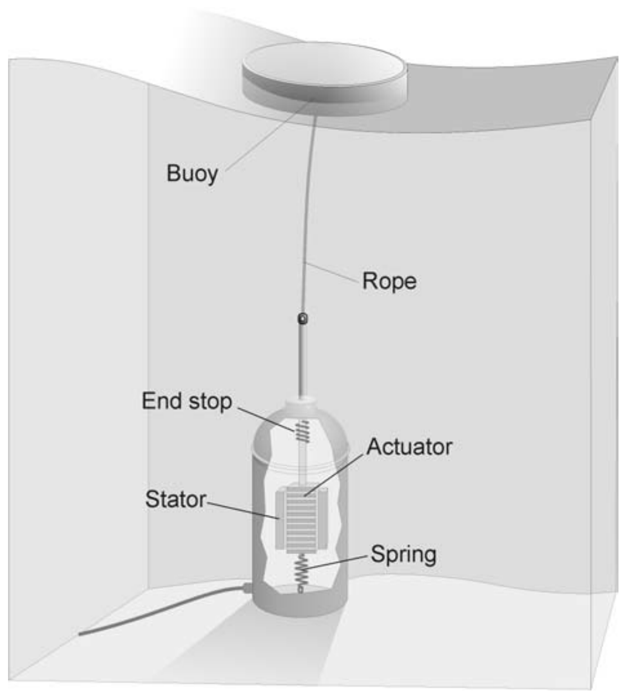

Figure 1.8: Linear permanent magnet generator used to convert ocean wave energy to electrical energy [13]

Figure 1.8 shows an example of a linear permanent magnet generator that could be scaled down and built into the frame of a backpack. The generator is of simple design and scavenges linear translational movement to create energy. The simplicity of a linear permanent magnet generator improves durability and reduces losses when converting mechanical energy to electrical energy.

1.5 Proposed Design

A suspended backpack energy scavenger was shown to be promising by Rome et al. [9], but there are some concerns over the durability and efficiency of the system. A combination of the suspended pack with linear permanent magnet generators, similar to wave energy converters, could improve durability and reduce potential inefficiencies of the design made by Rome et al. Figure 1.9 displays a model of the proposed design for an energy scavenging, suspended pack with linear permanent magnet inductive generators. The generator coils are enclosed within the pack saddle, indicated by (2), to protect them from environmental exposure as well as physical shock. A cutaway view of the proposed linear permanent magnet energy scavenger is shown in the inset window. The magnetic translators are encased in the tubular frame work. The pack would be suspended by a number of springs attached to the tubular frame that are not shown on the model. Bushings mounted in the pack saddle would provide low friction motion along the frame.

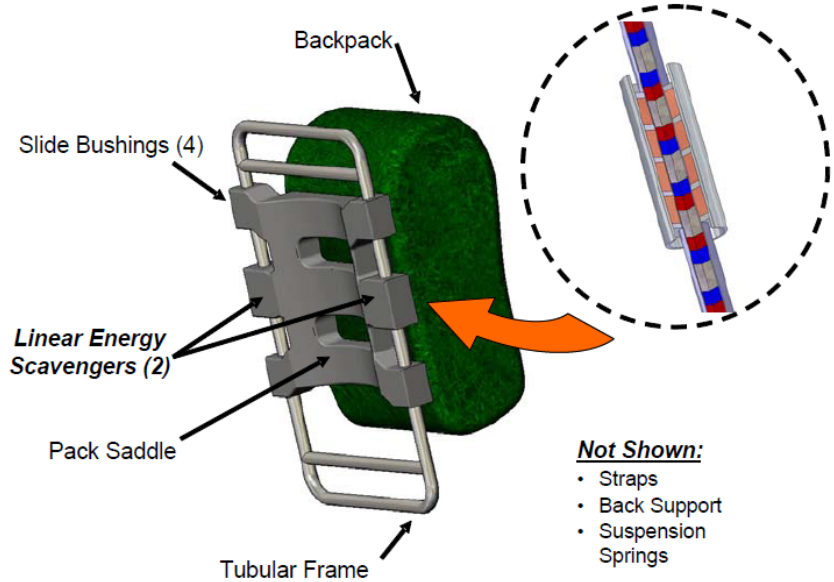

Figure 1.9: Suspended pack frame featuring magnetic stacks housed in tubular frame and stator coils enclosed in pack saddle

Unlike the rack and pinion system on the suspended pack frame of Rome et al. [9], a linear generator would not be externally mounted. The magnets and coils would be contained within the frame, protecting it from elements such as sand, water, dirt, and mechanical shock. By containing it inside the framework, the system would be more resistant to deformation of the tubular rails. As long as the pack frame is capable of oscillation, the generator would still function. With an exposed gear train, if the rack was moved or bent, the gears could bind and prevent relative movement. Without relative movement, the generator shaft would cease to spin, in turn causing the magnetic flux to stay constant, and no power would be generated. A linear generator could decrease inefficiencies in the system by eliminating a geared power train. While gearing provides the ability to increase speed or torque delivered to the rotary generator, it also produces power losses through the friction in the gear train. With an enclosed, lubricated system, these efficiencies can be minimized, but with a system open to environmental elements power losses can be large. Using a linear magnetic generator in a suspended backpack system similar to that of Rome et al., would simplify the system, improve efficiency and reliability, and increase energy conversion efficiency.

1.6 Thesis Layout

This thesis details the process of modelling, designing, fabricating, and experimentally testing a linear permanent magnet generator, designed to be used in a suspended frame backpack. The suspended frame backpack concept is based on the design made by Rome et al. [9]. For this proposed design the rotary generator would be replaced with a linear inductive generator to minimize power loss, increase reliability, and decrease complexity of the system.

Bateman [14] proposed a generator model by developing a mechanical vibration model based on base excitation to simulate the motion of the backpack, and adopting a magnetic model proposed by Baker [15]. The model used the Simulink software package to simulate the power output of the system. Using the model as a guide, a generator was designed. The Bateman model yields design parameters for the coil and magnet geometry. This thesis is designed to experimentally verify the model developed by Bateman, test the generator designed by Bateman, and propose an optimal linear generator design based on the results.

Chapter 3 presents the Bateman model [14] adopted from Baker [10]. Baker developed relations to predict magnetic flux radially away from the translator and force per coil, which are presented and discussed. The Simulink simulation developed by Bateman is presented and explained as well.

After the theoretical model is presented, the design and fabrication of a testing apparatus and experimental generators is discussed in Chapter 4. The design discussion covers theory and modelling the testing apparatus, power measurement circuit, and experimental generators. Fabrication techniques and materials used in the construction of the testing apparatus are briefly discussed. The techniques and materials used to build the generators is discussed in detail to explain the analysis incorporated within the design.

Following the design of the system, experimental results are presented in Chapter 5. The power generation of experimental generators are compared to the simulated values of the Bateman model to verify the accuracy of the model. Various designs are tested for power and voltage output of the generators. The generated power of the experimental devices is used to make comparisons for validation of Bateman's model, while the experimental voltage is tested as an important parameter to determine practicality of miniature linear generators.

The conclusions and proposal of future work are presented in Chapter 6. The validity of Bateman's [14] model designed for predicting power of linear permanent magnet generators is presented in this chapter and is based on the results of Chapter 5. The practicality of a linear generator used in a backpack frame to operate personal electronic equipment is shown. Finally, an optimal generator design is presented, and a proposal of future work needed to successfully develop a portable power system is made.

CHAPTER 2

BACKGROUND

The problem of generating power in remote areas has been outlined, and a proposed solution was presented. This chapter presents an overview of research conducted in the fields of walking gait kinematics, wave energy converters, and low temperature co-fired ceramics to support the development of the proposed solution. The research presented in this chapter shapes the design constraints, generator geometries, and preferred fabrication materials and methods used in this thesis.

2.1 Kinetics of a Typical Walking Gait

A simple model of a person's walking gait was developed by Saunders et al. [16]. Saunders et al. models the motion as if the leg of the foot planted on the ground were an inverted pendulum. When a person walks, they plant their foot on the ground, push their body up, and pivot over the foot. The other foot then gets planted as their body swings past the originally planted foot. Figure 2.1 show an illustrated picture of a person taking a step, highlighting the motion of the planted leg. The arrows depict the direction of travel of the person. An arc is outlined, by the dotted line, which represents the motion of the hip of the person as they move through the process of one step. The vertical displacement of the hip during the gait cycle is $5cm$ and is denoted as ΔH [9].

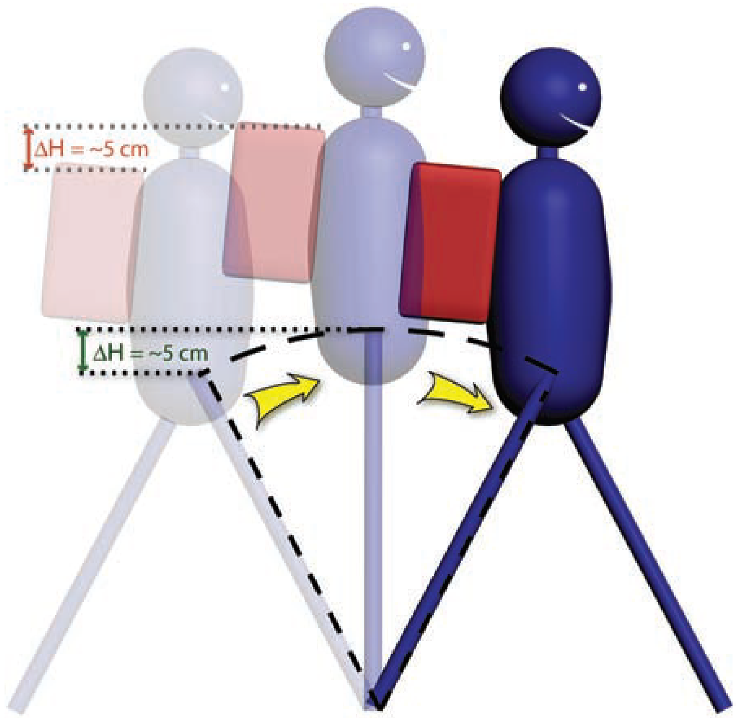

Figure 2.1: Picture of an animated person taking a step, highlighting the fact that the planted leg moves through a motion similar to an inverted pendulum [9]

By using inverted pendulum model, a sinusoidal motion of a person's, and in effect the backpack's, center of mass is achieved. This provides a convenient way to approximate the motion of a suspended backpack and was adopted by Rome et al. [9] and Bateman [14] for modelling a suspended energy scavenging backpack. The stepping frequency of a person walking is in the range of $1.7Hz - 2.3Hz$ [9, 17]. The vertical displacement of an average person as they take a step is considered to be $4cm - 7cm$ [9, 18]. The frequency of $2Hz$ and a vertical displacement of $1in$ ($5cm$) were used in the modelling and testing of the generators.

2.2 Wave Energy Converters

In order to directly harness energy from the motion of the oscillating backpack, a linear inductive generator is being proposed as a device to scavenge power. Wave energy conversion uses this type of generator to convert the energy from waves in the ocean into usable electricity as shown previously in Figure 1.8. Most consist of a buoy connected to a magnetic translator. The magnets are surrounded by a series of generators composed of wrapped, electrically conductive wire, denoted as the stator or stator coils. As the waves rise and fall, the buoy causes the translator to oscillate through the stator coils. As the translators move, the magnetic flux within each stator coil changes due to the relative motion between the two components. The changing magnetic flux couples with the wire and causes current to flow through the wire.

There is much research being invested in developing this technology because there is a large movement to develop energy sources that use fuel sources other than fossil fuels. Ivanova et al. described an octagonal shaped linear permanent magnet generator to decrease power fluctuations and suppress voltage harmonics [19, 20]. Figure 2.2 displays a cross-sectional view of one proposal of an octagonal shaped linear permanent magnet generator. The translator is made up of eight rectangular magnets inside of the stator coils. The windings on the stator coils are wound parallel to the face of the magnet in a manner that will cause the magnetic field to flow perpendicular to the windings.

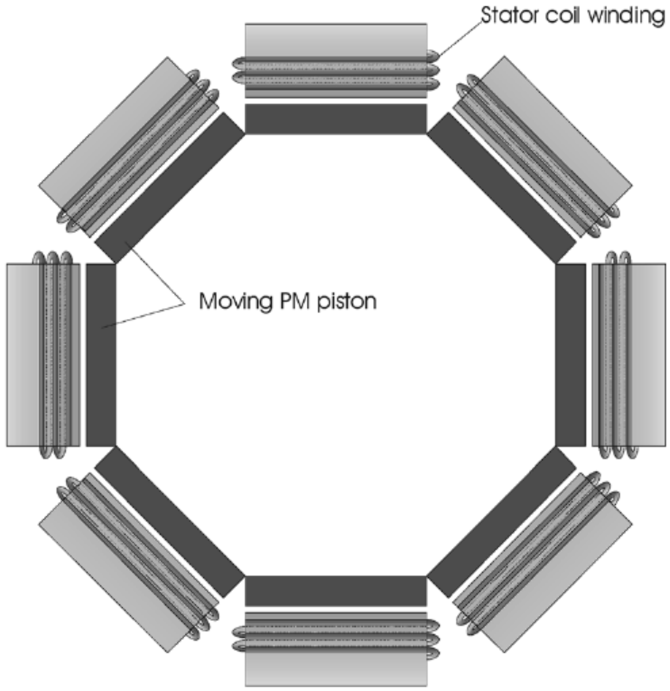

Figure 2.2: Cross-sectional view of an experimental, octagonal linear permanent magnet generator examined in an attempt to decrease power fluctuations and suppress voltage harmonics in wave energy harvesting [19]

Wang et al. [21] modelled and prototyped a miniature, $15mW$ generator for use in small electronics such as "self-winding" watches. A prototype of the device made by Wang et al. is shown in Figure 2.3. The translator can be seen in the upper-right potion of the picture, the stator coils are housed in the disk located nearest to the ruler. This device is designed to produce $15mW$ of power when running at 6000rpm. This is a rotary generator but is based on a similar concept to the linear wave generators through its ability to harness mechanical energy from harmonic motion and convert it directly to electrical energy.

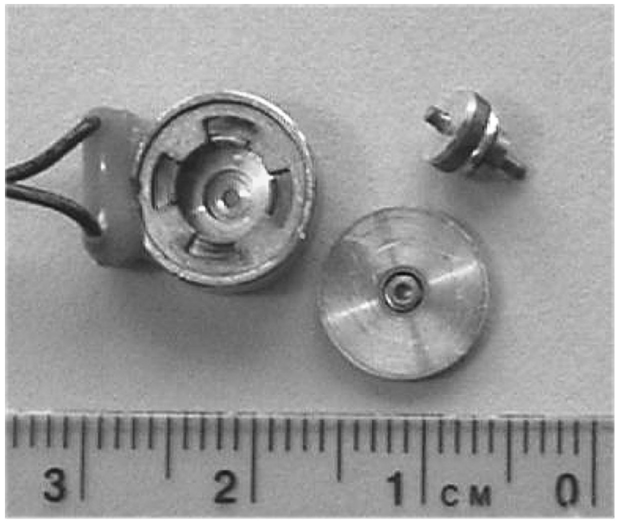

Figure 2.3: Prototype of a miniature permanent magnet generator used for applications in small electronics requiring less than $15mW$ of power [21]

Danielson et al. and Baker et al. have have described linear generators that are fundamentally similar to the proposed generator of this thesis, but are much larger in scale [10, 11, 13, 15, 22]. These papers explore various configurations and modelling techniques of linear permanent magnet generators. Of particular interest are Danielsson's and Baker's work on air-cored permanent magnet tubular linear generators [10, 13]. Figure 2.4 displays the generator in a linear air-cored induction generator. The isometric picture in the upper-left corner is a view of the magnetic stack and coils together. The stator coil is label in the picture as a large white ring surrounding a stack of alternating white and black disks. The windings of wire are located within the ring. The diagram at the bottom of the image shows a cross-sectional view of the magnetic translator. The translator consists of alternating magnets and steel spacers stacked on a center shaft, as indicated by the alternating black and white disks in Figure 2.4. Four small arrows, and the N and S symbols denoting north and south power, are located on the surface of each magnet in the diagram near the bottom of the image. These arrows indicate the direction of the magnetic field. It can be seen that the direction of the magnetic field of each consecutive magnet is reversed. The curved arrows at the boundary of the stack are representative of the shape of the magnetic field. The device geometry is characterized by several dimensions, including: W_m is the magnet width, W_p is the spacer width, R_i is the inner radius of the stator coil, and R_o is the outer radius of the stator coil. During operation, the translator will oscillate back and forth through the stator coil. The magnetic field inductively couples with the conductive wire in the stator and causes current to flow through the wire.

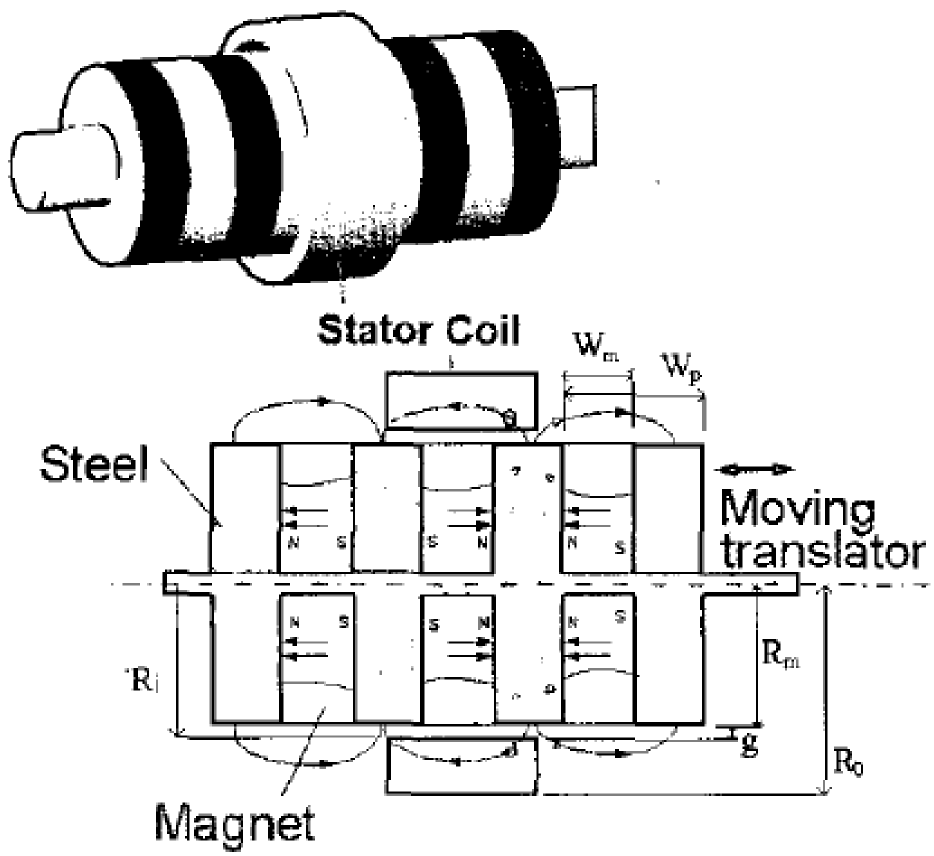

Figure 2.4: Diagram of a linear air-cored permanent magnet induction generator [10]

Linear generators generally have an iron, or steel, sleeve encompassing the stator coils to create a consistent magnetic field along the entire width of the stator coils. A system with a ferrous metal surrounding the stator coils is called an iron-cored generator. The ferrous metal surrounding the coils will polarize with the magnet in the translator, which has a conditioning effect of the magnetic field. A cross-sectional view of a linear generator with a steel sleeve is shown in Figure 2.5. The steel sleeve is labelled stator steel and is located on the opposite side of the stator coils from the magnet. The flux paths are shown as a solid line running through the magnets between the wires and through the stator steel. The flux paths are shown going in a nearly straight path from the magnet to to the stator steel, illustrating the conditioning of the field. The dashed red line indicates the magnetic path with no steel surrounding the stator. When no steel is present, the generator is called an air-cored generator. The strength of the magnetic field of an air-cored generator weakens as it gets further from the magnet. The field strength of the iron-cored generator is constituent of the entire breadth of the coils.

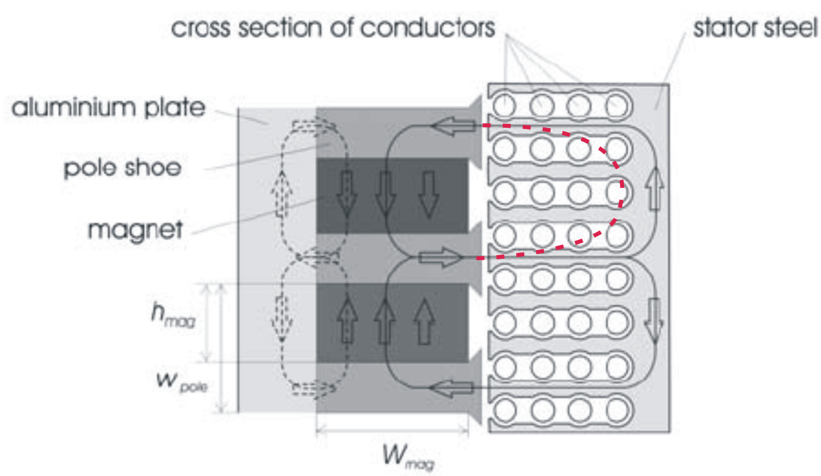

Figure 2.5: Cross-sectional area of an iron-cored linear permanent magnet generator, illustrating magnetic flux paths [23]

The air-cored design is less widely used, but is desirable for a suspended backpack generator because it will have less mass than a traditional iron-cored generator. As the backpack will be carried by a person and scavenging energy from their muscles, a lightweight design is preferable. A drawback to the air-cored design is that it will not generate as much electricity as the iron-cored.

2.3 Low Temperature Co-Fired Ceramic

The generator will be subjected to harsh environments that could cause failures to sensitive electrical equipment. Low temperature co-fired ceramic (LTCC) is a material that could be used to build the stator coils to provide added durability and coil density. LTCC is provided in thin sheets purchased from DuPont. LTCC 951 Green Tape^{TM} is composed of alumina, low temperature glass, and an organic binder [24]. While in the green, unfired state, the LTCC materials can be machined and printed with electrical circuit elements. The LTCC sheets can be connected through layers by way of vias, which are vertical holes through layers of LTCC. The vias are filled with conductive material. Figure 2.6(a) shows a layer of LTCC with printed circuitry, including vias to connect consecutive layers. The light gray line that curves down the left side of the disk is electrically conductive paste that has been applied to the surface of the LTCC layer, the four light gray, round, pads indicate vias that provide electrical connections between the layers.

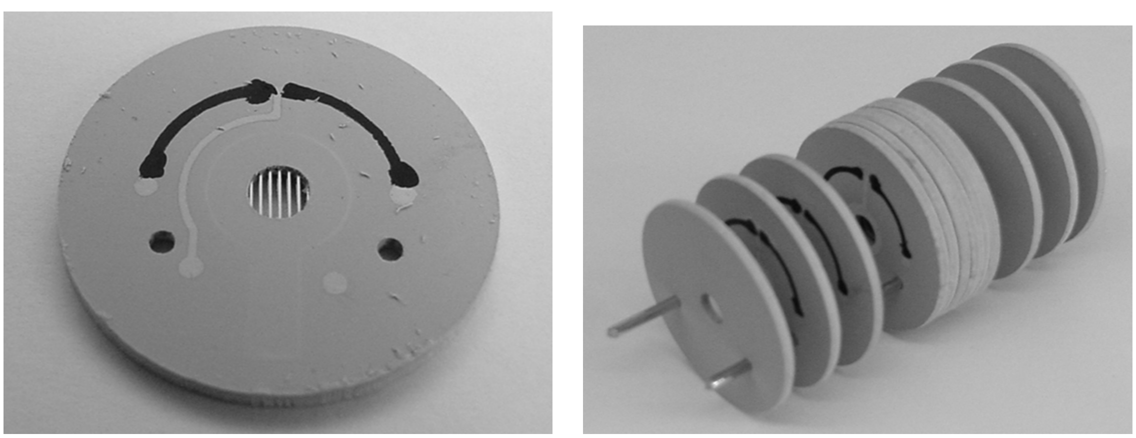

(a) Sample of printed LTCC showing printed circuitry and embedded equipment

(b) Multiple layers of an ion mobility spectrometer being collated using two guide pins

Figure 2.6: Two views of an ion mobility spectrometer designed using LTCC by Plumlee et al. [25]

By developing the stator coils with printed and layered LTCC materials, the generator would be more resistant to natural elements and frictional wear. When the system of printed LTCC layers is fired, the low temperature glass within the ceramic melts and fuses between the separate layers, merging them into one single piece of material, thus providing a hermetically sealed generator [24]. This provides protection from water, sand, and any other element that might be encountered while installed in a backpack. While in the field, it is possible that the frame could get deformed, which could cause rubbing to occur between the magnets and stator coil. The ceramic would be able to withstand the rubbing without concerns of the wires becoming exposed.

The fabrication process is shown in Figure 2.7. As can be seen, the start of the process is forming the blank and preconditioning it. Preconditioning consist of cutting the sheets of LTCC into the correct size and shape, installing any embedded hardware, as seen in the center of the disk in Figure 2.6(a), and cleaning the surface to ensure no debris is on it. After preconditioning, it is recommended that the via holes are created on all layers. After vias are formed, they should be filled with conductive material, then the conductive circuit should be printed on the surface of all layers of the ceramic. The next step is to collate and laminate the layers of ceramic. The layers are aligned using guide pins as seen in Figure 2.6(b), then they are laminated at a pressure of approximately $20000kPa$. After lamination, the stack of LTCC is then fired in a furnace at $850C^{\circ}$ for 20 minutes. The last step in the process is post-fire processing, which includes connecting electrical interconnects to interface with the internal circuitry of the LTCC device.

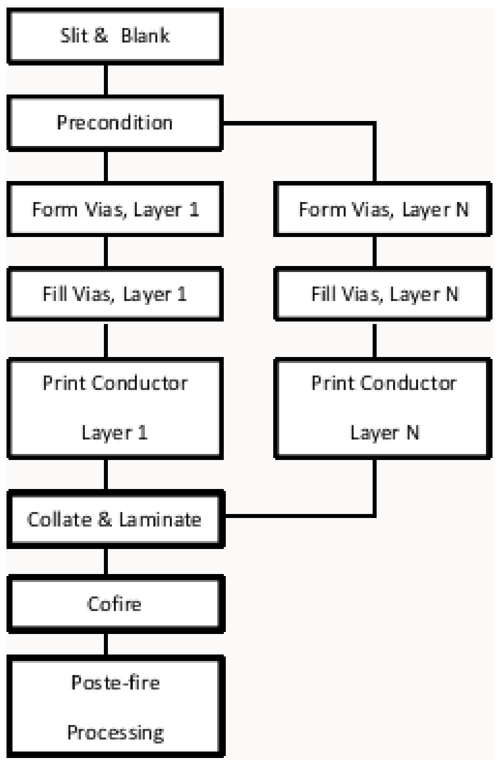

Figure 2.7: A flowchart depicting the typical process involved when printing circuitry and firing 951 Green Tape^{TM} LTCC [24]

CHAPTER 3

DESCRIPTION OF THEORETICAL MODEL AND PRELIMINARY RESULTS

Bateman began the development of an energy scavenging suspended backpack with linear inductive generators. She proposed a stator coil and magnetic translator design, developed an analytical model to predict the performance of the system, and developed an analytical model to predict the power produced by the system [14]. Much of the coil design and analytical model were adapted from the work of Baker [15], Wang [21], and Baker et al. [10] on design of tubular air-cored permanent magnet generators for marine energy converters. The mechanical model was based on a base excitation vibrations model developed by Bateman [14].

3.1 Simulink Power Model

3.1.1 Mechanical Model

A Simulink model, shown in Figure 3.1, was developed by Bateman to determine the maximum power output of a miniature linear permanent magnet generator [14]. The model predicts the kinetic energy of the system, and the resistive force applied by the induced magnetic field of the stator coils. The input was set using a MATLAB script that Bateman wrote and the outputs were saved as MATLAB matrix files.

The parameters and model inputs are defined via a MATLAB script, which must be run before the simulation is initiated. The parameters of the system are shown in Table 3.1.

Table 3.1: Model parameters and inputs used to simulate the power generation of linear permanent magnet generators

Parameters	Inputs
Spring Constant	Oscillation Amplitude
Friction Damping	Oscillation Frequency
Load Mass	Load Acceleration

With the given parameters, the model calculates the net force on the backpack and the relative velocity of the backpack. To calculate the net force on the backpack, the resistive force of the induced magnetic field in the stator coils, referred to as the magnetic coupling force, is required. A function, adapted from Baker [15], calculated the force from the stator coils based on the relative velocity of the backpack and the position of the stator with respect to the translator. The velocity, backpack mass, and magnetic coupling force are then used to calculate the instantaneous power generated by the stator coil and kinetic energy of the system. The magnetic coupling force, instantaneous power generated by the stator coil, and kinetic energy are all written to matrix files to be analysed in MATLAB.

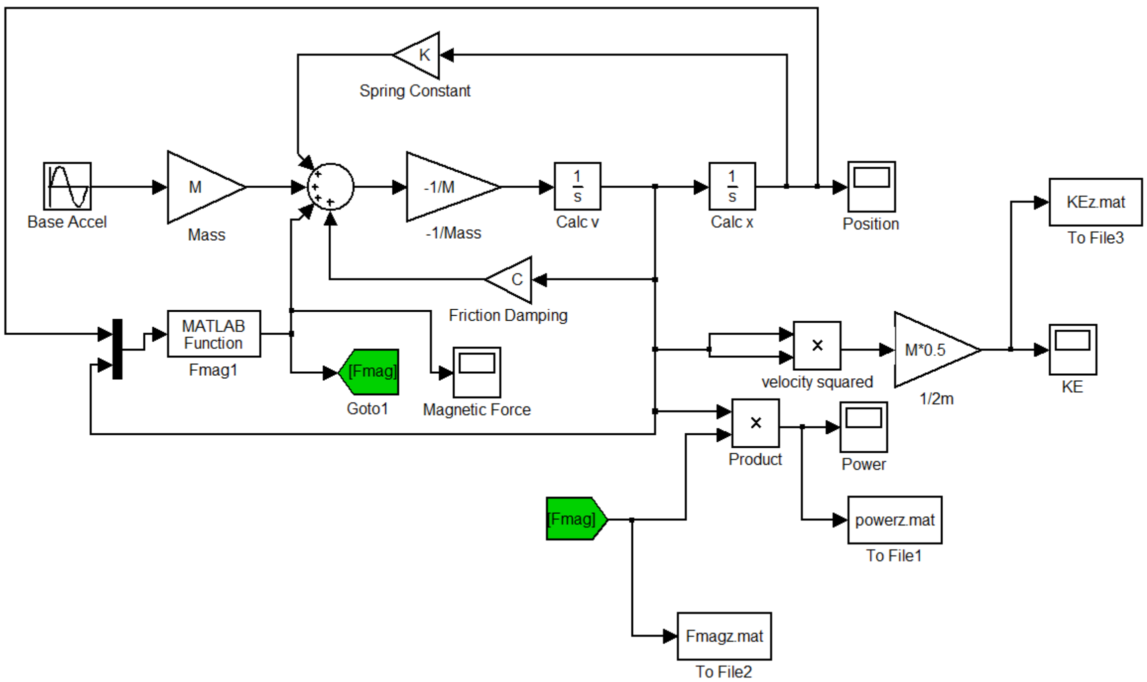

Figure 3.1: Original Simulink Model Developed by Bateman to Determine Power Output of Generator [14]

This model uses $2Hz$ walking frequency and $5cm$ vertical displacement of load as parameters. It also requires inputs that were presented in Chapters 1 and 2, which are listed as follows:

- Weight of the pack ($28kg$)
- Linear spring constant ($8000\frac{N}{m}$)
- Friction damping coefficient ($189.315\frac{kg}{s}$)

The spring constant and damping coefficient were values determined by Bateman [14] to yield optimal relative velocity of the backpack with respect to the person.

The model performs calculations over a time interval of $5s$ with a time step of $10ms$. The magnetic force, spring force, and friction force are used to calculate the net force on the system, as can be seen by the feedback loops shown in Figure 3.1. The main function of this model is to predict the maximum power output of a given linear inductive generator in the suspended backpack, based on the kinematics of the person walking and the load that they are carrying. Being able to input a given generator, backpack loading, speed of movement, and predict the power provides a method that can be used to design an optimal generator for a range of conditions that could occur in real-world applications.

3.1.2 Magnetic Coupling Between Translator and Stator Coils

The magnetic force is based on Baker's work in modelling a tubular air-cored linear permanent magnetic generator to scavenge energy from the motion of waves in the ocean [15]. Of specific importance are the equations used to calculate the magnetic force of the stator due to inductive coupling between the wire and the permanent magnets. The MATLAB function in the Simulink simulation, shown in Figure 3.1, uses these equations to approximate the force on the translator from the induced magnetic field in the stator coils. The calculations done in the MATLAB function are presented in Equations 3.1 through 3.6. The coupling force produced by a segment of stator wire per unit volume is given by 3.1. The force is a function of the current density (J), equivalent magnetic flux density (B_g), and geometry relationship between the stator and translator. Solving Equation 3.1 for force and integrating over the volume of the stator coils yields the force per stator as shown in Equation 3.2 where a stator is considered to be a single generator consisting of a series of coils, wrapped in the same direction.

$$\frac{F}{vol} = JB_g e^{\frac{-r+R_m}{l_g}} \tag{3.1}$$

$$F_{coil} = \int_0^{2\pi} \int_{R_i}^{R^o} \int_0^{C_w} J\hat{B}_g e^{\frac{-r+R_m}{l_g}} r dz dr d\theta \tag{3.2}$$

Where: Vol Volume of space stator coils occupy (m^3)

J Current density ($\frac{Amp}{m^2}$)

$\hat{B}_g$ Maximum magnet flux density at surface of translator (T)

r Radial distance from translator (m)

R_m Radius of ring magnet (m)

lg Length of air gap (m)

R_o Outer radius of stator coils (m)

R_i Inner radius of stator coils (m)

C_w Width of coil windings within stator (m)

Baker [15] developed a relationship to approximate the magnetic flux experienced by the entire volume of the stator coil without having to use finite element analysis to predict the decrease in magnetic field. Equation 3.3 calculates a theoretical maximum surface flux density that can be used to approximate the magnetic flux experienced by the stator coils. It is based on the geometry of the stator coil, magnets, and steel spacers.

$$\hat{B}_g = \frac{\pi B_r R_m w_m}{2\mu_r R_m (W_m + W_s) + \pi W_m W_s} \tag{3.3}$$

Where: B_r Remnant flux density of the magnet (T)

W_m Width of ring magnet (m)

μ_r Relative permeability

W_s Width of steel spacer (m)

The actual flux density varies along the longitudinal axis of the translator surface. The variation in flux density is modelled in the simulation Equation 3.4 where x is the longitudinal position of the stator with respect to the translator in meters.

$$B_a = \hat{B}_g \sin\left(\frac{\pi x}{W_m + W_s}\right) \tag{3.4}$$

To approximate the peak current density, Bateman developed Equation 3.5 [14]. It is dependent on the geometry of the stator, resistance of the wire, and relative velocity of the backpack with respect the person. This relationship is used to predict the amount of current per unit area that will be generated by the stator.

$$J = \frac{v L_p^2 B_a e^{\frac{-r+R_m}{l_g}}}{R_{sis} Vol} \tag{3.5}$$

Where: v Instantaneous velocity of translator ($\frac{m}{s}$)

L_p Path length of wire within stator (m)

R_{sis} Internal resistance of stator coils (Ω)

Substituting Equations 3.3, 3.4, and 3.5 into Equation 3.2 and integrating it yields an equation that was used to calculate the coupling force per coil, which is displayed in Equation 3.6. This is the output of the MATLAB function in the Simulink simulation that was developed by Bateman.

$$F_{coil} = \frac{\pi C_w v L_p^2 B_a^2 l_g \left[2R_i + l_g - (2R_o + l_g) e^{-\frac{2(r+R_m)}{l_g}}\right] e^{-\frac{2gap}{l_g}}}{2 R_{sis} Vol} \tag{3.6}$$

3.2 Stator Coil Design Proposed by Bateman

Bateman [14] proposed a design for a miniature translator and stator coil, which was adapted from work done by Baker [15]. The translator is composed of a series of ring magnets with reversed polarities stacked on a central shaft and separated by steel spacers.

Figure 3.2 displays an experimental translator on the left and Bateman's SolidWorks model representing the translator on the right [14]. The red disks in the SolidWorks model indicate the north pole of the magnets and the blue disks represent the south pole. The magnets and steel spacers have a 2.54cm outer diameter, a 0.79cm inner diameter, and 0.63cm thickness.

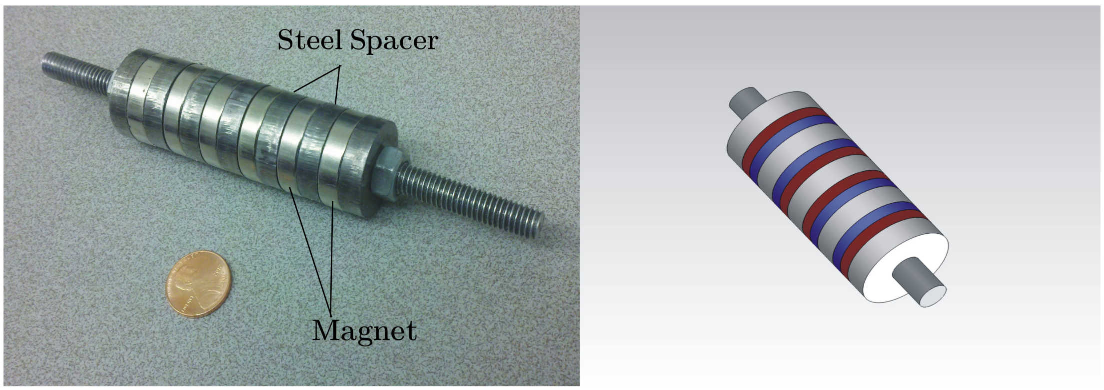

Figure 3.2: SolidWorks assembly of Bateman's proposed translator next to a picture of the experimental translator [14]

Bateman proposed a stator coil design and simulated it using the Simulink power model [14]. Bateman designed and fabricated this coil using LTCC as a substrate, and silver paste as the internal conductor. The stator coils were 1.12cm wide, had an inner radius of 1.29cm, and an outer radius of 2.37cm. The coil contained 480 windings and was predicted to have an internal resistance of 10$Ohms$.

Figure 3.3 shows the LTCC coil design. The large blue disks represent layers of LTCC and the silver paste is shown as silver spirals on the disks. During fabrication of the stator, the LTCC disks would be pressed and fired to create bonds between the layers. The conductive coils are electrically connected by vias filled with silver paste.

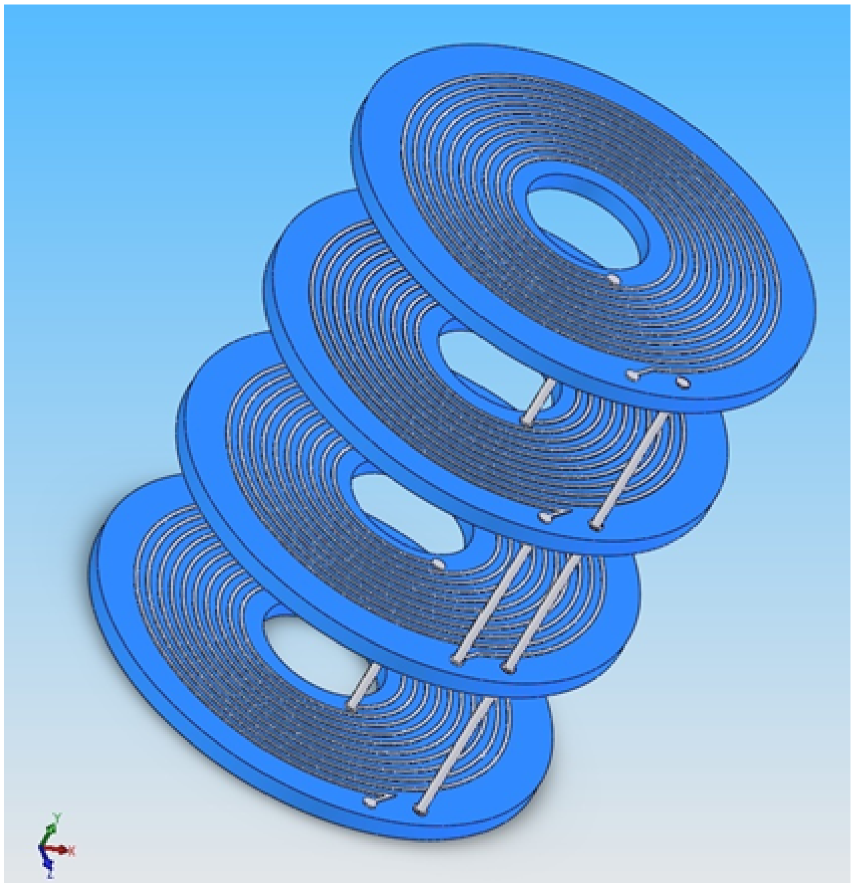

Figure 3.3: Original Design of Coils Using LTCC and Silver Paste

3.3 Model Results

Bateman [14] simulated the proposed generator to predict the power generation of the system, and the coupling force of the stator coil. The generated power and the coupling force were saved and analysed using MATLAB to determine, qualitatively, if the simulation provided a good approximation. The simulation approximated $2s$ worth of data to ensure any steady-state operation of the generator.

Figure 3.4 is a plot of the power that was predicted from the simulation of Bateman's proposed generator. The plot shows instantaneous power (W) as a function of time (s). This plot displays the absolute value of the power while in a real system this type of generator would produce alternating current. The peak amplitude of the power is approximately $4.5W - 5W$. The plot contains seven cycles of data made up of four power spikes. Each group of data peaks represents half a period of movement of the backpack. Transient responses can be seen in the first half second of data, denoted by the changing amplitude of the signal. After the transient response dies out, the amplitude of the cycles are constant, which illustrates steady-state.

The middle peaks of each cycle have the largest amplitude because the velocity of the system is at a maximum at the center of the oscillation. Starting at the bottom of its movement, the backpack will accelerate upward, reaching a maximum velocity at the midpoint of the oscillation. As the pack moves through the midpoint of oscillation, it loses velocity, coming to a stop at the top the oscillation. The changing amplitude of power within each cycle reflects the velocity change of the backpack because the energy generation of an inductive generator is dependent on changing magnetic fields. More energy will be produced as changes in magnetic flux increase. At the start and finish of each period of oscillation, the velocity of the backpack goes to zero. Without motion in the backpack, the stator experiences no change in the magnetic flux. This is reflected as the valleys, where power equals zero, between each cycle.

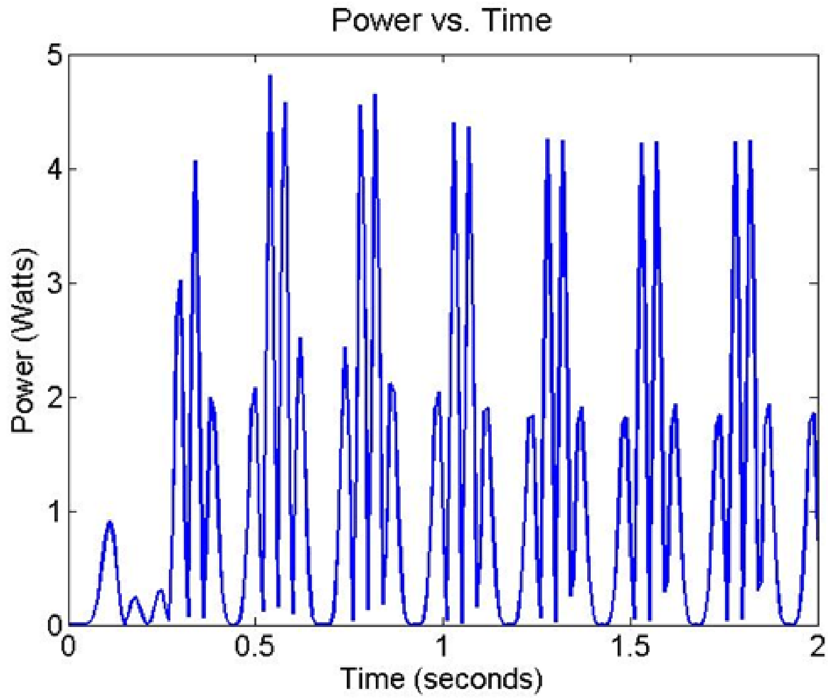

Figure 3.4: Plot of power from a generator over a period of two seconds [14]

The change in velocity is displayed by the changes in power magnitude but the harmonic nature of the signal is due to polarity changes of the magnets. The oscillation of power generation within each cycle is due to the reversed polarity of each consecutive set of magnets. At the center of each pole, the power will approach zero because all of the magnetic flux will be parallel to the motion of the generator, causing the stator coils to experience no change in magnetic flux. When the pole change approaches the stator, the power spikes because the magnetic field is perpendicular to the stator coils, causing large changes in magnetic flux through the coils.

Bateman analysed the coupling force of the stator coils to determine if it would add a significant burden to a person using the device. Figure 3.5 show a plot of coupling force. The force is shown on the vertical axis in Newtons and time is shown on the horizontal axis in seconds. This plot shows similar qualities to Figure 3.4 such as cycles of force correspond to changing velocity of the system and harmonic variation in the force due to changing polarity. The peak amplitude of the coupling force is $15N$. The magnitude of the magnetic coupling force alternates between positive and negative in each cycle, which is indicative of the changing motion of oscillation.

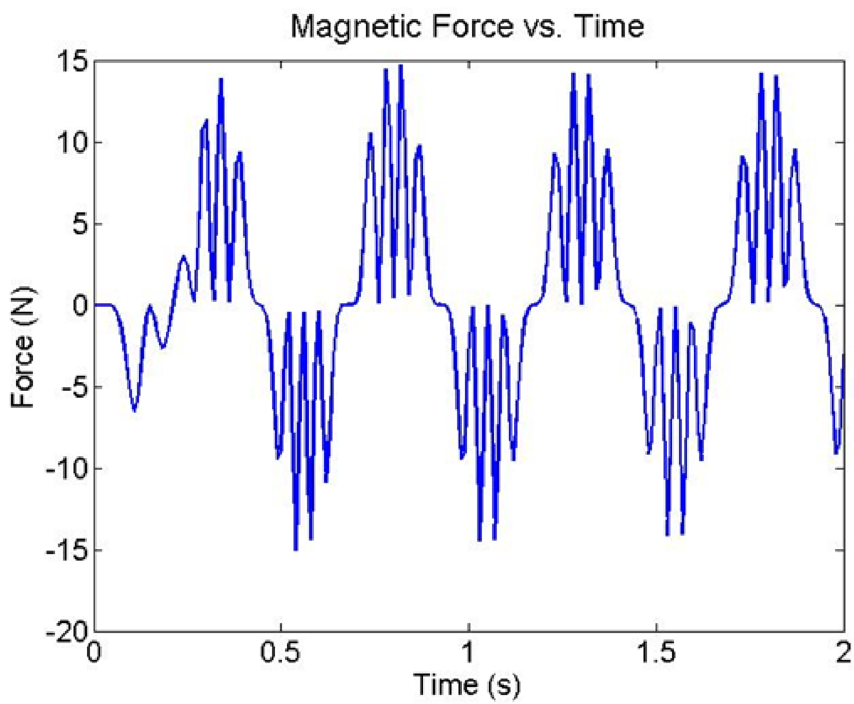

Figure 3.5: Plot of coupling force between stator coils and magnetic translator, as a function of time [14]

The force show in Figure 3.5 is due to the magnetic field in the stator coils generated when current flows through the wire. This force is important because if it becomes greater than the force from the weight of the load, the pack will cease to move independent of the person. If the backpack is unable to move relative to the person, no energy will be generated. Another concern is that as force increases the generator will draw increasingly larger amounts of energy and fatigue the person using the device. The combination of the magnetic coupling force and the weight of the device is desired to be under $58.86N$ to attain the desired weight reduction presented in Section 1.1.

Based on the power and coupling force curves created by Bateman [14], the model predicted data that agreed with the physics of the system. It captured the changing polarity of the magnets in the translator and the changing velocity of the backpack relative to the user. It was designed to predict the power generated from the tubular air-cored linear permanent magnet generator and would not be useful in predicting power generation for other linear generators. A qualitative comparison of the model results to experimental data was not performed by Bateman. Chapter 4 details the design and fabrication of an experimental testing apparatus, as well as experimental stator coils, to be used in the validation of Bateman's Simulink model.

CHAPTER 4

DESIGN AND FABRICATION OF TESTING APPARATUS AND GENERATORS

In order to accomplish the validation of the model, a test stand, and experimental generators were designed and fabricated. Constraints were of the translator and stator coils were presented in Chapter 3. A testing apparatus was designed based on a system that oscillates at a specific frequency and has a set amplitude. A measurement circuit was developed to provide optimum resistance to obtain maximum power transfer from the stator coils. The input of the testing apparatus consists of the forcing frequency of the oscillations, amplitude of oscillations, and magnitude of load resistance.

4.1 Parameters Used to Develop Testing Methods for Model Validation

A standard testing process was designed to obtain experimental results that would be used to determine the validity of the Simulink model. Power was the most important variable to be tested. A resistive circuit was designed to measure the voltage of the generator and calculate the dissipated power. The experimental results are compared with output from Bateman's model to validate the accuracy of the model. Figure 4.1 shows the circuit that was used to measure and calculate generated power. The circuit includes a power source and three resistances. The three resistances correspond to the internal resistance of the generator, a resistor with a constant resistance ($500m\Omega$ Resistor), and a variable resistor (25Ω Potentiometer). A dash block encloses the section of the circuit corresponding to the stator coil. The internal resistance causes a loss of power through the coils, leaving the usable generated power to be dropped across the $500n\Omega$ resistor and the potentiometer. Voltage measurements are taken across the two external resistors, enabling the power and current to be calculated. By placing two resistors in series, it allowed the resistance of the potentiometer to be calculated based on the current flowing through the $500m\Omega$ resistor. This was determined to be the most accurate method of measuring the resistance of the potentiometer.

It was important to accurately measure the resistance of the potentiometer to ensure the maximum power generation of the generator. The maximum power generation occurs when the load resistance is equal to the internal resistance of the generator. The potentiometer was used to vary the load resistance to ensure it was equal to the internal resistance.

The magnetic flux was an important constraint in experimentally determining the power generation capacity of the device. The coupling force used to calculated the generated power is a function of the magnetic flux. To ensure the approximation developed by Baker, an AlphLab Inc. DC MAGNETOMETER was used to map the maximum field strength of the translator from the surface to $35mm$ radially outward from the magnets. By comparing the measured field with the approximations made based on Baker's work, it will indicate if the Simulink model is reliably predicting the magnetic flux that is experienced by the stator coils [15].

In order for the system to be viable, a minimum peak voltage of $3V$ is desirable. The generated alternating current will need to be rectified to be stored in a battery. A common method of rectification consists of passing the current through a forward bias diode, which will only allow a positive voltage through. A drawback to diode rectification is it requires

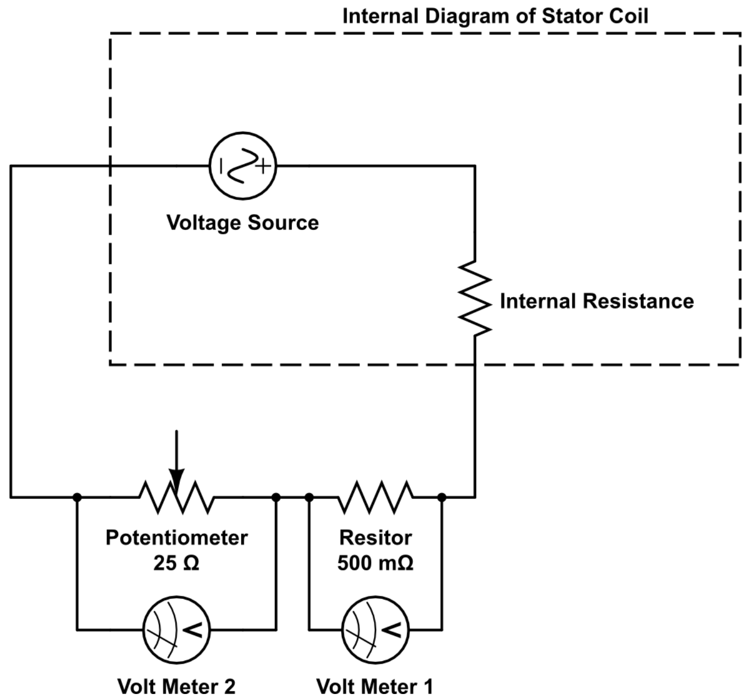

Figure 4.1: A resistive circuit designed to measure and calculate the generated power from an experimental linear inductive generator

a voltage drop to activate the diode. If the generated voltage is close to or less than the voltage needed to activate the diode, all of the power will be dissipated in the rectification process and will not be available for use.

In order to obtain accurate comparisons, the testing apparatus needs to drive the oscillation of the system at the same frequency as the model. To accomplish this, a control system was developed to force a 12V DC motor to operate at a user-chosen angular velocity that corresponded to the required frequency. The controller was developed using LabVIEW software, an H-Bridge, and a National Instruments USB-6211 data acquisition board. A testing apparatus and coils were designed and built based on the given requirements and deliverables. The materials and designs are discussed further throughout the remainder of this chapter.

4.2 Test Stand

4.2.1 3D Modelling and Description

An apparatus was designed to simulate the motion of a the suspended backpack, which is excited by the vertical travel of the wearer while walking. The testing apparatus contains a magnetic translator, stator coils, a drive system, a speed controller, and a data acquisition system. A schematic of the testing apparatus and connections is displayed in Figure 4.2. The computer runs a LabView simulation, which has three purposes. Its first purpose is to collect the voltage across the resistors and calculate the dissipated power. The second is to collect data from a quadrature encoder on the motor to determine the frequency of the oscillations. The last function is to use the measured angular velocity of the motor as an input to a PI controller, which then outputs a duty cycle to the data acquisition board. The data acquisition board interprets the duty cycle and pulses an H-bridge on and off to control the frequency of the motor via pulse width modulation.

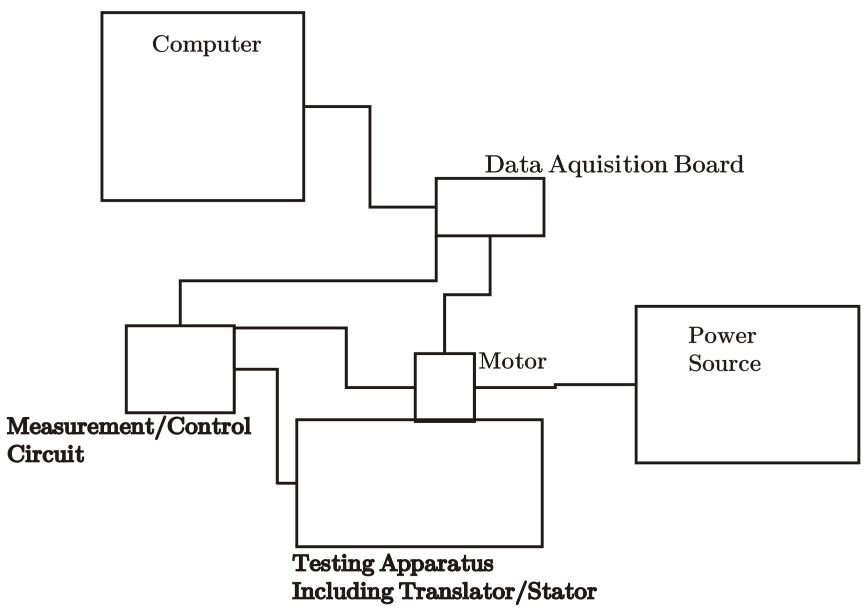

Figure 4.2: Schematic displaying the various components of the testing apparatus and the electrical connections to all of the components

The motor shaft is connected to a scotch yolk mechanism used to turn rotation into harmonic linear oscillation. Figure 4.3 is a schematic depicting the operation of a scotch yolk mechanism. The motor shaft connect in the center of the scotch yolk, and the translator is connected to the oscillating bar. The stator is mounted to the base of the testing apparatus to constrain it from moving as the translator oscillates. Conductive leads are connected from the stator coils to the measurement circuit as depicted in Figure 4.2. The measurement circuit has leads on either side of the two resistors that connect to terminals on the data acquisition board, allowing the measured voltage to be sent to the computer.

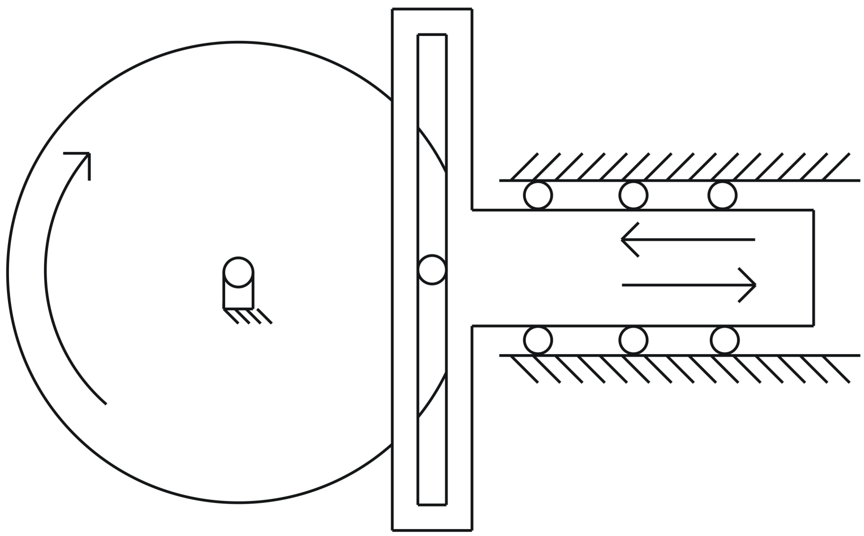

Figure 4.3: Schematic of a scotch yolk mechanism used to convert rotation to linear oscillations

Figure 4.4 shows an isometric view of a 3D CAD model of the testing apparatus. The two black sections represent linear bearings of the scotch yolk mechanism. The magnetic translator is indicated by the alternating white, red, and blue disks attached to the large horizontal bearing. The blue disk located at the end of the L shaped support and surrounding the magnetic translator is the stator coil. As the apparatus moves, the magnetic translator will oscillate horizontally while the stator coils are held stationary in the fixture.

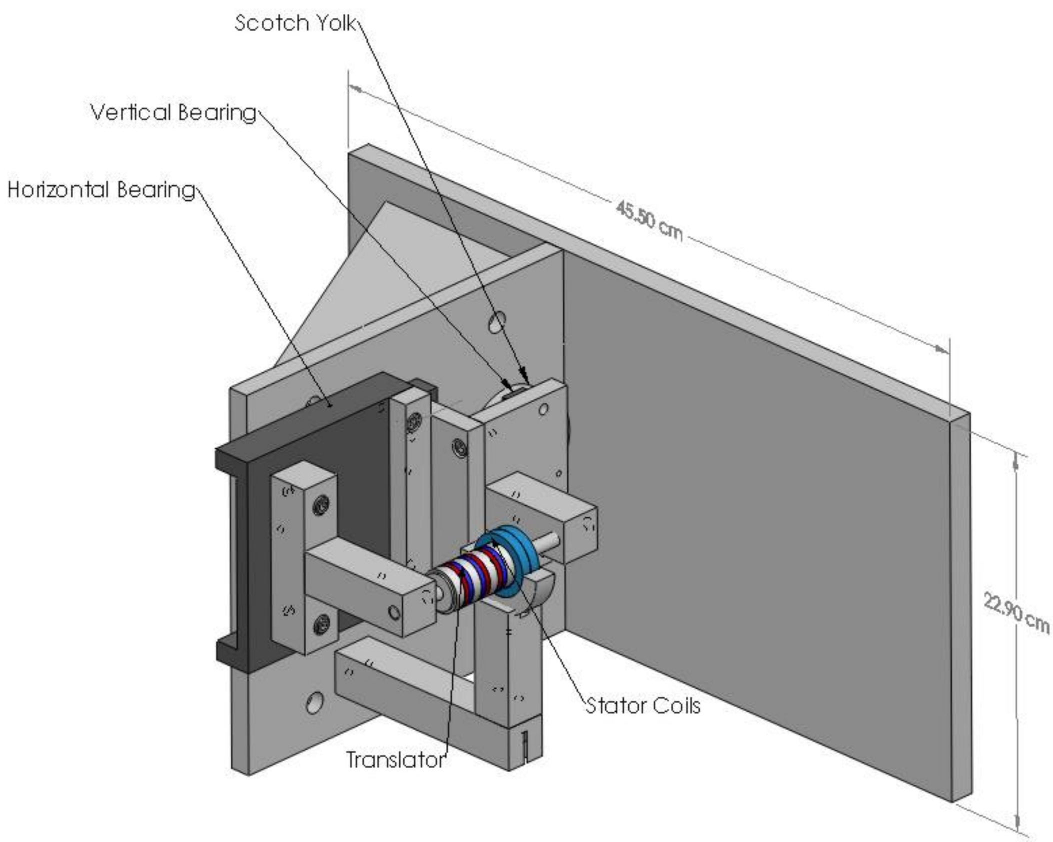

Figure 4.4: SolidWorks assembly of test apparatus without controller or data acquisition systems

Figures 4.5 and 4.6 display the apparatus at the two extreme positions of translation. The blue highlighted disk represents the scotch yolk that works in unison with vertical and horizontal bearing to convert the rotary motion of the motor into linear motion. The two positions indicated display the peak displacement where velocity goes to zero and the apparatus begins moving in the opposite direction. The scotch yolk is highlighted and labelled, as is the point of connection between it and the linear bearing. The offset from the center of the scotch yolk defines the amplitude of motion of the magnetic translator.

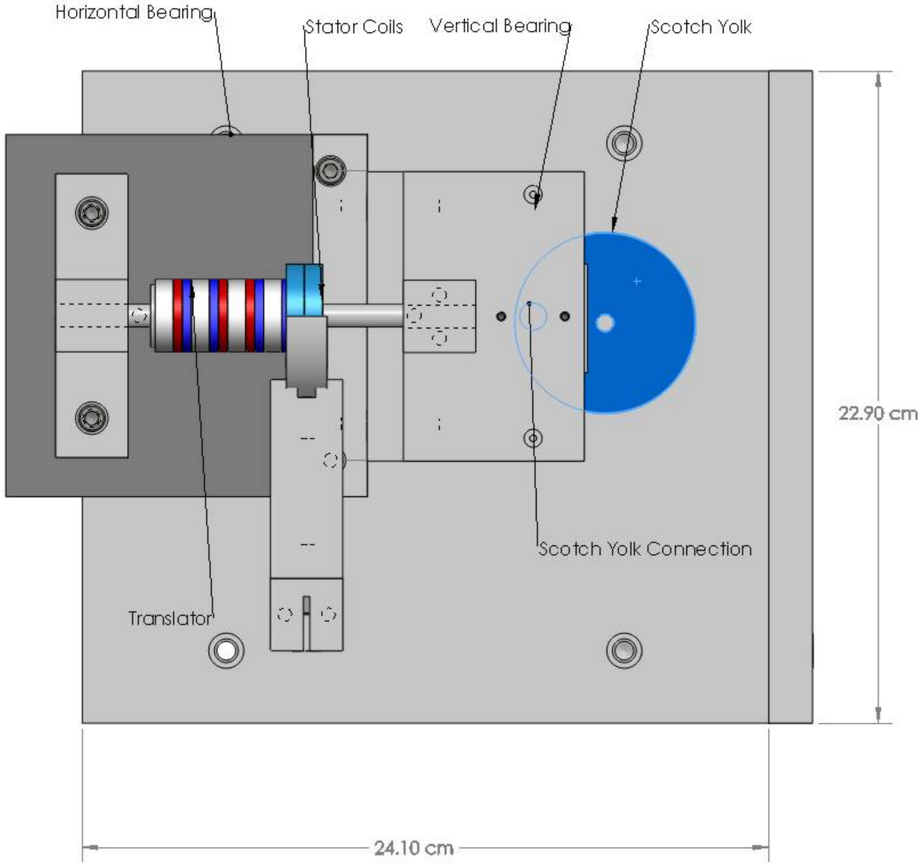

Figure 4.5: 3D CAD model of testing apparatus in a fully extended position

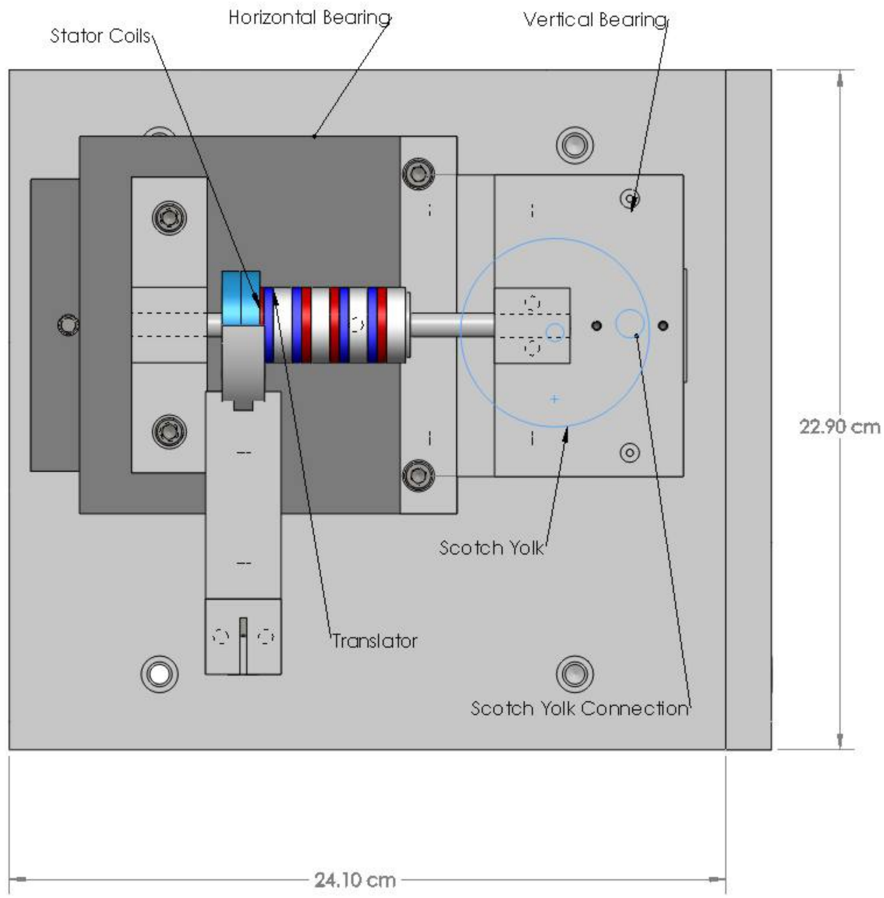

Figure 4.6: 3D CAD model of testing apparatus in a fully retracted position

4.2.2 Materials and Fabrication

The base of the testing apparatus, as well as the mounting brackets, are made primarily from aluminium and were custom fabricated on the campus of Boise State University. The two bearings are comprised of Parker linear slides. The custom fabrication was completed using a combination of a CNC mill and a manual lathe. The motor used to drive the motion is a Pololu 67:1 Metal Gear motor with a 64 count per revolution encoder connected to the drive shaft.

4.2.3 Motor Control System

The frequency of the oscillation period was the desired input to the testing apparatus because the step frequency is used as a controlling input in Bateman's model [14]. The testing apparatus motor was equipped with a quadrature encoder, which allows the motor velocity and frequency to be determined. One revolution of the motor shaft creates one period of motion of the testing apparatus, thus the frequency of the motor rotation is equal to the oscillation period frequency. Pulse width modulation set using a digital controller was chosen as the method to control the motor frequency.

A proportional plus integral (PI) controller is used to modulate the frequency of motion of the device. Originally, a proportional controller was tested, but was found to allow large steady-state errors in the motor frequency. The PI controller was chosen to damp out oscillations in the steady-state frequency. The controller was designed in the LabVIEW software package and uses the trapezoidal rule to approximate the integral of the error. Equation 4.1 calculates a duty cycle to be sent to the DAQ board, based on the difference in user set frequency and measured motor frequency. D is the duty cycle. D_o is the duty cycle of the previous iteration of the program, k_p is the proportional controller constant, k_I is the integral controller constant, f_o is the frequency of the test stand on the previous iteration of the program, and f is the current frequency of the test stand. Equation 4.2 shows the trapezoidal rule used to approximate the integral [26].

$$D = D_o + k_p(f_o - f) + k_I(f_o - f)dt \tag{4.1}$$

$$f(y)dy \approx \frac{\Delta y}{2}(f(y_{i-1}) + f(y_i)) \tag{4.2}$$

Figure 4.7 displays the motor control portion of the LabVIEW program. The controller reaches the steady-state frequency in approximately 0.8s. There are minor oscillations when the system is running at the steady-state frequency. The program calculates the duty cycle value to be written to the motor using the two boxes marked Proportional and Integral. The Proportional box calculates the $k_p(f_o - f)$ term in Equation 4.1 and the Integral box uses Equation 4.2 to calculate the $k_I(f_o - f)dt$ term in Equation 4.1.

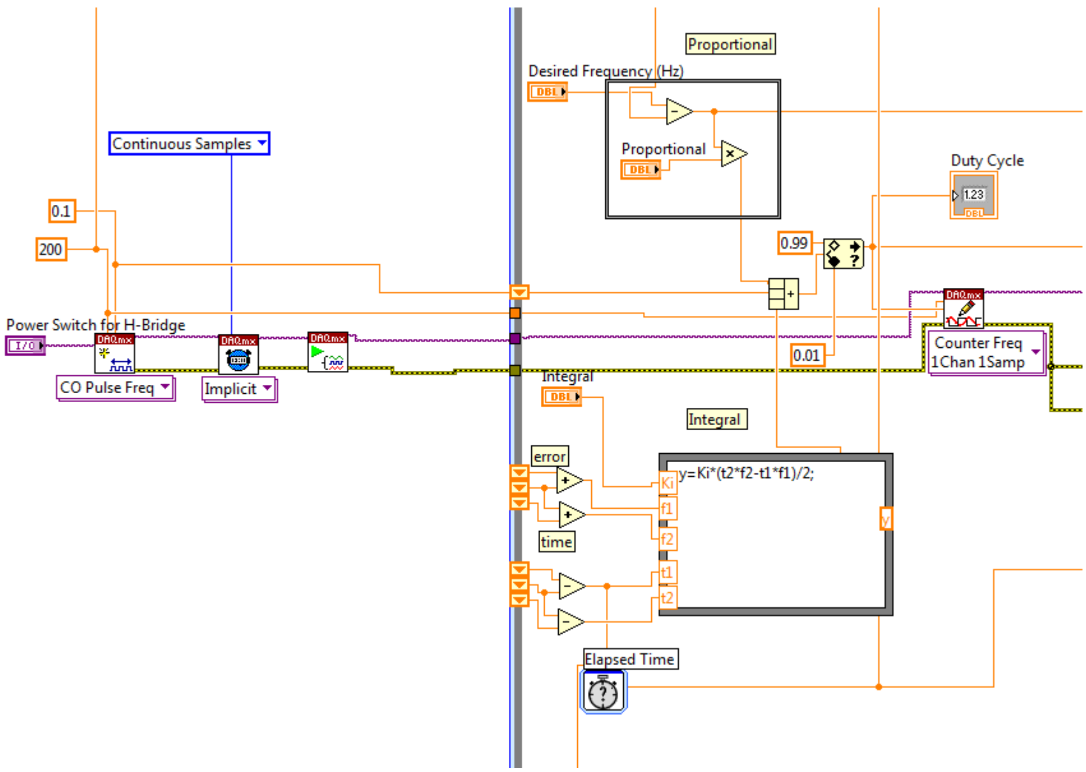

Figure 4.7: Portion of LabVIEW Code Functioning as a PI Controller

The oscillations of the frequency are likely due to the momentum change of the testing apparatus as the oscillations change direction of travel. Figure 4.8 displays the calculated linear momentum change of the apparatus as a function of time. The momentum oscillates in a range from +/–56.5$\frac{kg*m}{s}$. It can be seen that within a quarter of a second the momentum is forced to change from 56.5$\frac{kg*m}{s}$ to -56.5$\frac{kg*m}{s}$. At steady-state the frequency oscillates within +/–0.2Hz.

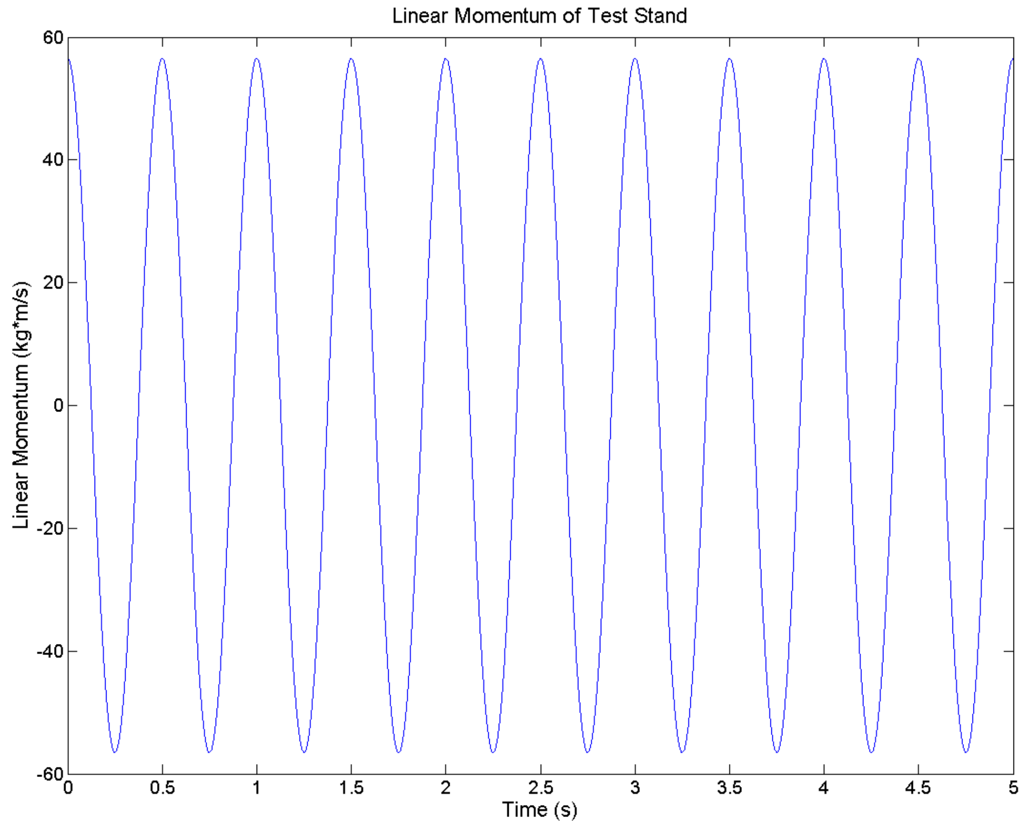

Figure 4.8: Linear Momentum of Test Apparatus as it Oscillates

Pulse width modulation (PWM) is the method used to control a motor by sending pulses of power equating to a percentage of time, duty cycle, will remain on. A PWM signal was generated using a pre-designed duty cycle signal within LabVIEW, which can be seen in Figure 4.7 labelled as CO Pulse Freq. The PWM signal was sent through a data acquisition board into a set of Texas Instruments SN754410NE 16 pin H-bridges. The H-bridge functioned as an on/off switch that allowed power to the motor based on the pulse length of the PWM. The program refreshed at a rate of $200Hz$, causing the pulse length to be $5ms$ in length. This means that if the PWM sent out a duty cycle of 70%, the motor would be on for $3.5ms$ and off for $1.5ms$ every pulse cycle.

4.2.4 Generator Measurement System

A measurement system was designed to obtain the voltage potential, current, and maximum power transfer from the generator. This was accomplished by measuring the voltage across a series of a resistor and a potentiometer via the data acquisition board. The resistor has a resistance of 0.5Ω while the potentiometer has a variable resistance in the range of 0Ω to 25Ω. To calculated the power (P) generated, the voltage (V) was measured across the resistor, and ohms law, shown in Equation 4.3, was used to calculate the generated current (I). The voltage drop across the potentiometer along with the current were used to calculate the exact value of the potentiometers resistance. Using the total resistance (R_{tot}) of the circuit, Equation 4.4 was used to calculate the power.

$$V = I * R \tag{4.3}$$

$$P = I^2 R_{tot} \tag{4.4}$$

The variable resistor is useful for finding the optimum resistive load for power generation with an inductive generator. The maximum power transfer law states "the load resistance that absorbs the maximum power from a two-terminal circuit is equal to the Thevenin resistance" [27]. The generator is considered a two-terminal circuit where the Thevenin resistance is equal to the internal resistance of the coils. The potentiometer was used to match the load resistance with the internal resistance of the generator, allowing maximum power transfer to occur.

4.2.5 Completed Test System

Figures 4.9 and 4.10 show the assembled testing apparatus, measurement circuit, control circuit, and data acquisition board. The fixture used to hold the stator in place was modified from the original design for ease of changing stators. Figure 4.9 shows a view of the front of the testing apparatus. One of the magnet stack supports was removed and the mounting hardware for the coils was modified from the CAD model shown in Figure 4.4. These modifications eliminated the need for tools when removing and replacing the stators. The motor, encoder, and wiring connections can be seen in Figure 4.10. All of the data transfer was done using the National Instruments USB-6012 data acquisition board shown in Figure 4.10. A Hewlett-Packard 6652A DC power supply was used to provide power to the motor.

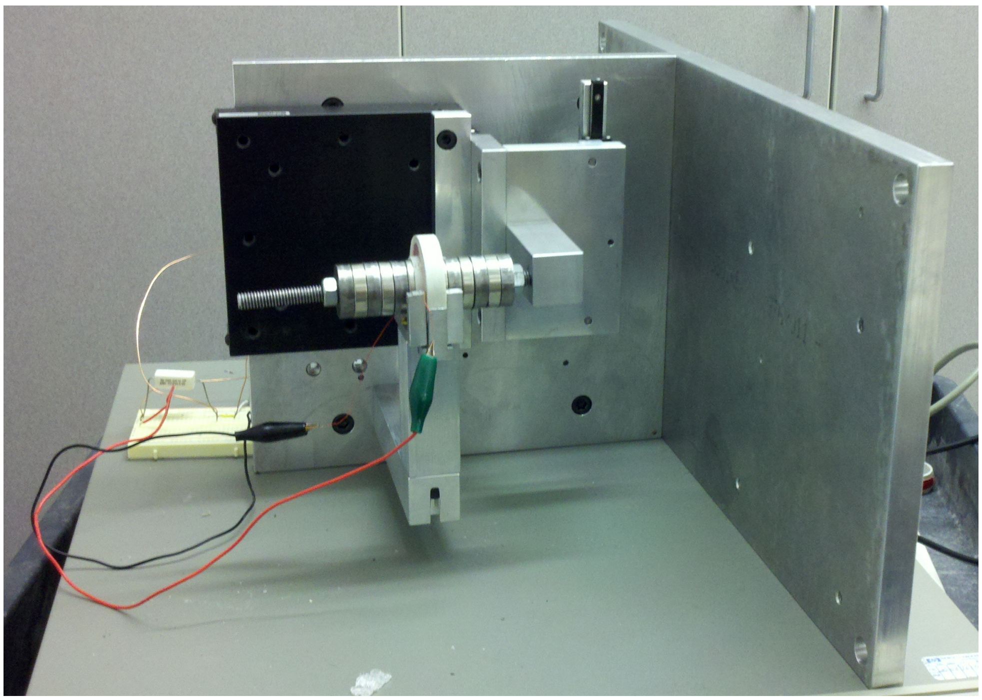

Figure 4.9: Photograph showing a frontal view of the experimental testing apparatus

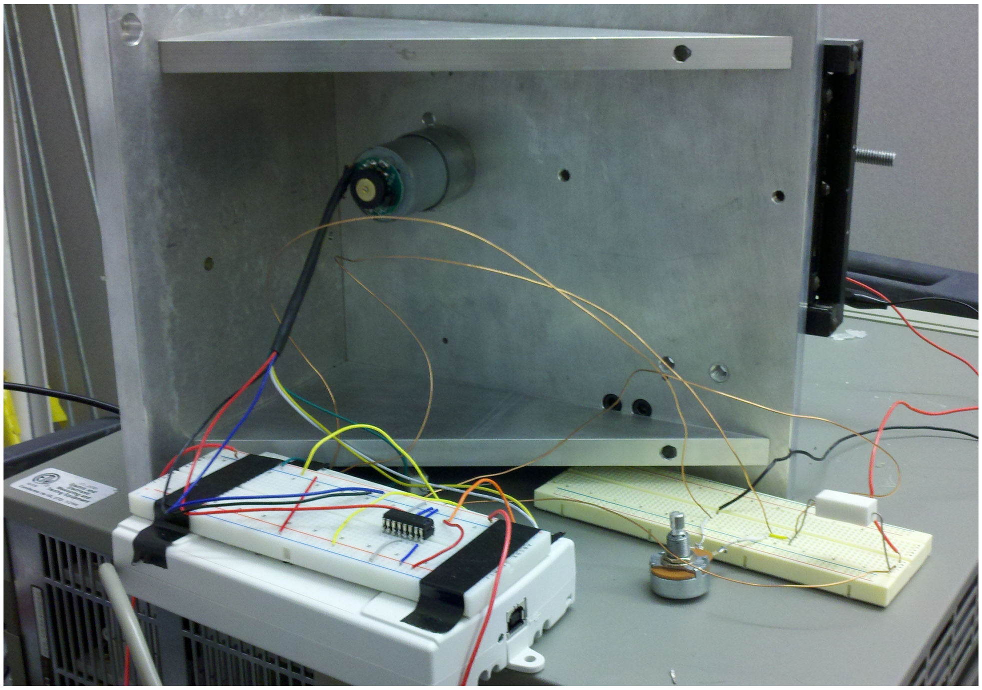

Figure 4.10: Photograph showing a rear view of the experimental testing apparatus including the measurement circuit, control circuit, motor, and data acquisition board

The generator testing apparatus is capable of maintaining a frequency in the range of $1.5Hz$ to $2.5Hz$. It has the capacity to test generators with a minimum internal resistance of 0.5Ω and a maximum resistance of 25.5Ω. It was successful in simulating an oscillatory movement at an average frequency of $2Hz$ as displayed in Figure 4.11. The spring and damper systems of the backpack were not included, which necessitated modifications to the Simulink model designed by Bateman [14]. The model was designed as a base excitation system but the testing apparatus is a directly driven system.

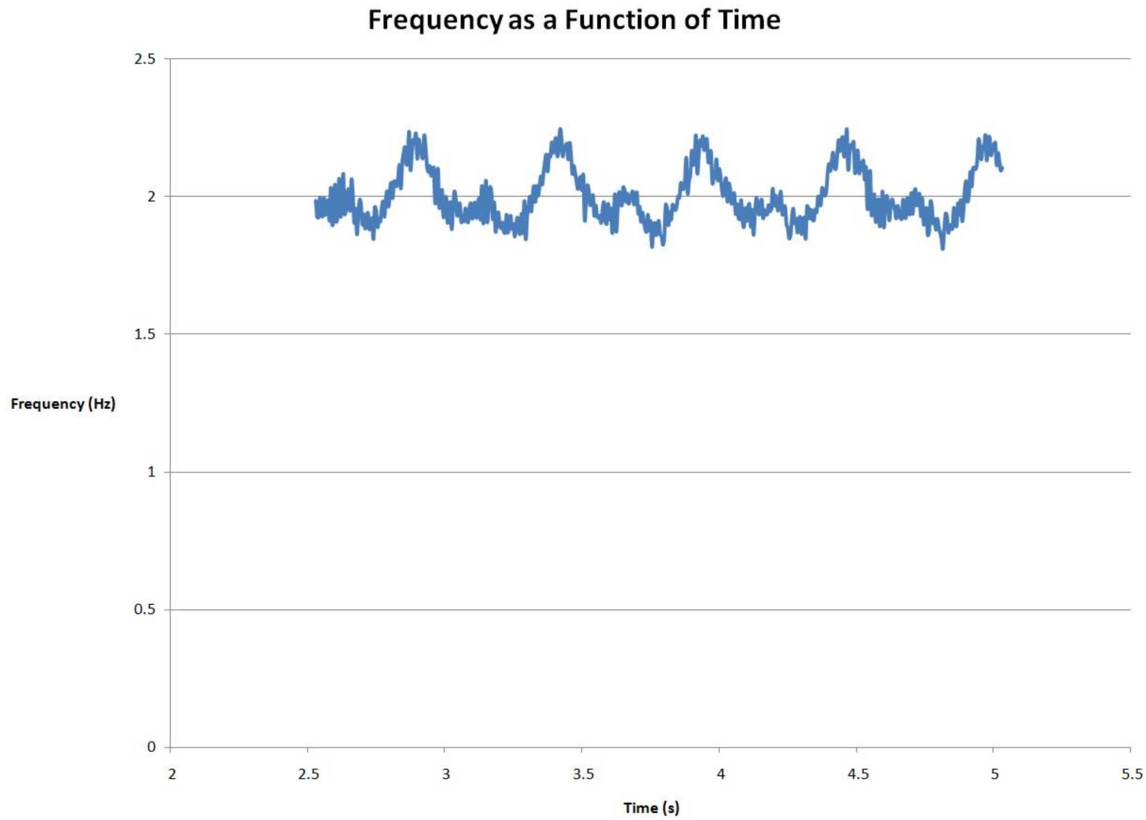

Figure 4.11: Plot of experimental frequency as a function of time while operating at a frequency of $2Hz$

4.3 Stator Design

4.3.1 Materials

An experimental stator design was proposed by Bateman [14] as discussed in Chapter 3. The stator width was proposed to be equal to the width of one magnet plus one steel spacer. It would contain 480 turns of wire, and have a radial thickness (coil height) of $6.65mm$. Three coils of this design were fabricated using LTCC with printed silver paste making up the conductive wires. During testing, it was found that this design did not produce any useful power and that it was difficult to ensure that the generator contained no short circuits, or open circuits. To ensure the coil was conductive, experimental stator fabrication was done using readily available materials and common fabrication processes to verify the results of Bateman's model.

Schedule 40 polyvinyl chloride (PVC) tubing with a one-inch inner diameter was used to act as the structure when winding stator coils. It was desirable to minimize the distance from the magnetic stack to the coils of wire, therefore the PVC was custom turned to have a thickness of $1mm$. Magnet wire was used for the conductive windings of the generator. Magnet wire is single-core copper wire that has a very thin polyurethane insulation to ensure tight packing when winding inductors. In order to ensure the Simulink model would accurately predict values when stator geometry was changed, three sizes of wire were used to create a range of coils to test. Four stators were fabricated, none of which contained matching geometry and wire size, to ensure the simulation was tested for a large range of stator geometries. Table 4.1 shows the specifications of each of the coils along with names that will be used to refer to the stator being discussed.

Table 4.1: Names and specifications of four stators designed and fabricated to verify Bateman's model

Stator Name	Wire Size	Coil Height	Coil Width	Number of Windings	Internal Resistance
Stator A	30 awg	3.8mm	12mm	480	19Ω
Stator B	30 awg	6.65mm	5.6mm	340	15Ω
Stator C	26 awg	8.58mm	4.6mm	193	3.4Ω
Stator D	20 awg	10.8mm	6.45mm	60	0.5Ω

The number of windings was not consistent between the stator designs because the changes in wire diameter dictated how many windings could fit in the specified coil area. Stator A had a small coil height and large coil width when compared to Stators B through D. The coil height of the stators progressively increased in order to test the accuracy of Bateman's simulation as the stator coils were placed in regions of weak magnetic field. At a large distance away from the magnet, the wires will no longer experience any changing magnetic flux due to a weakening magnetic field and will fail to induce current. When no current is induced, the coils experiencing no magnetic flux change will add electric resistance to the system without generating power. Power will be lost due to inherent resistance in the wire.

4.3.2 Fabrication

A coil winder was fabricated, as shown in Figure 4.12. The winder consists of a wooden dowel to hold a spool of wire, $\frac{5}{8}$" steel all thread to hold the core as the coils are wound around it, and a Vernier photo-gate to record the number of windings. A household drill with a $\frac{1}{2}$" chuck was connected to the all thread to spin the PVC to wind the wire around it. The photo-gate sent a signal to the computer through a Vernier Labpro, and a gate counter indicated the number of revolutions made. This was developed to allow fast and consistent construction of generators, to minimize counting errors, and to improve reproducibility during the validation of the model.

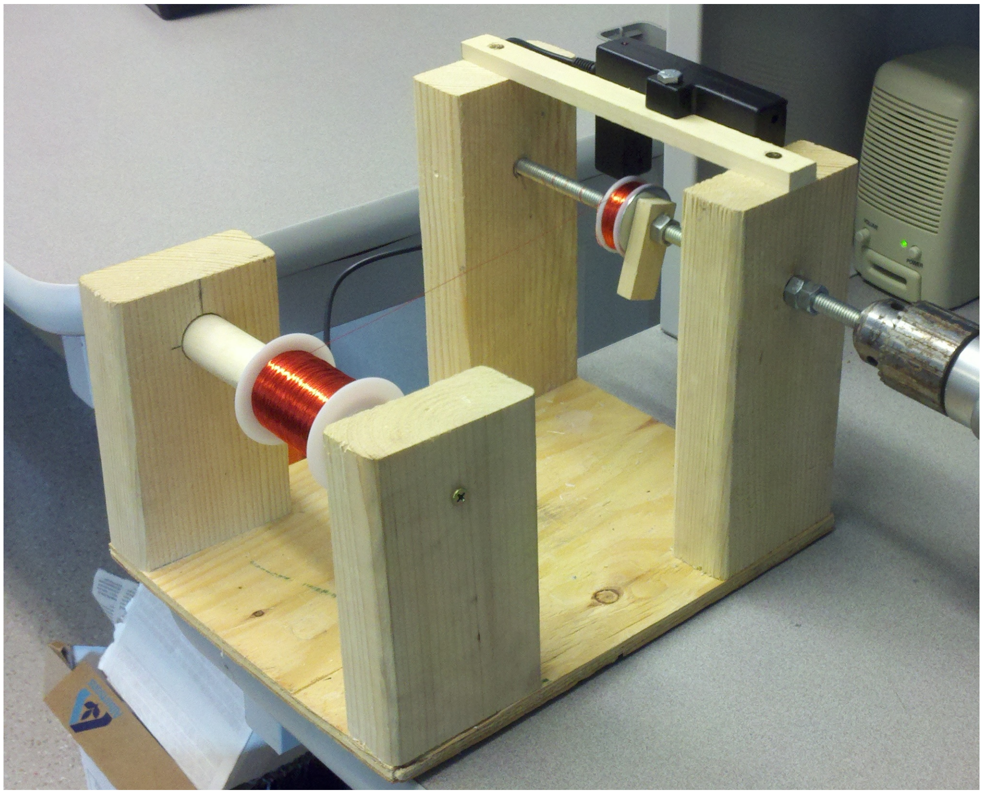

Figure 4.12: Custom Designed Coil Winder for the Construction of Test Generators

After developing an experimental apparatus, stator tests were performed to measure the power, voltage, and current of the stators. These tests were compared to the simulation developed by Bateman [14] to determine the accuracy of the model results. It is desired to have a simulation to predict an optimum stator design in the process of designing an energy scavenging backpack that uses linear permanent magnet generators. The following chapter presents the results of the experimental testing, and compares the experimental data with the model results.

CHAPTER 5

TESTING AND RESULTS

5.1 Preliminary Testing

Testing was done on the experimental stators, shown in Table 4.1, to determine generated power and voltage of each. The results of the experimental testing were compared to the results from Bateman's model to determine the accuracy of the model results. The first coil tested was fabricated using LTCC, and was found to be non-conductive. The fabrication process of the experimental stators was adjusted, as presented in Chapter 4, to guarantee stator conductivity. An inability to match a standard magnet wire diameter to the size of the printed circuit on the LTCC ceramic Stator A does not have the same geometry as the stator proposed by Bateman.

Figure 5.1 shows a picture of Stator A which contains red wire 30awg magnet wire and has a coil width of $12mm$. Coils were fixed in place using plastic disks and epoxy. The wire was wound with a packing factor of approximately 0.42, which indicates that 42% of the area that the area containing the wire is filled with coils, and 58% is filled with air. The insulation is thin and is included in the diameter of the wire, further decreasing the packing factor of conductive material. A good packing factor, acquired by a machine wound stator, would be approximately 60%, with a maximum of 78.6% [28].

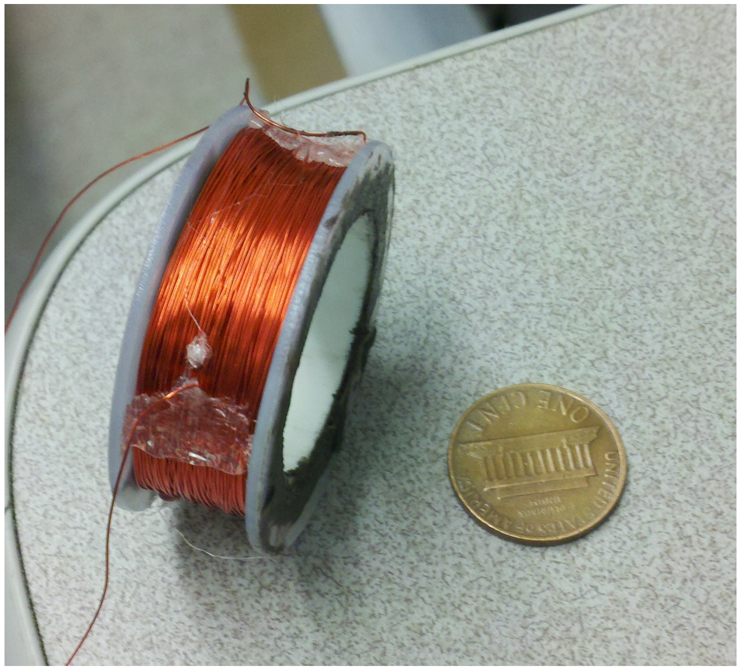

Figure 5.1: Picture of Stator A

Figure 5.2 shows the generated power magnitude, of Stator A, predicted by Bateman's model. The plot shows the power in watts on the vertical axis and time in seconds on the horizontal axis. It is similar to the original plot as seen in Figure 3.4. The maximum power generated is $4.8W$. As was discussed in Chapter 3, the absolute value of power is displayed in the plot. The timespan of the plot is two seconds, displaying the initial transient response damping out. This happens within approximately one second. Cycles of oscillation occur every $0.25s$. Each cycle indicates the translation in one direction of travel of the testing apparatus, with each peak indicating a change in magnetic polarity.

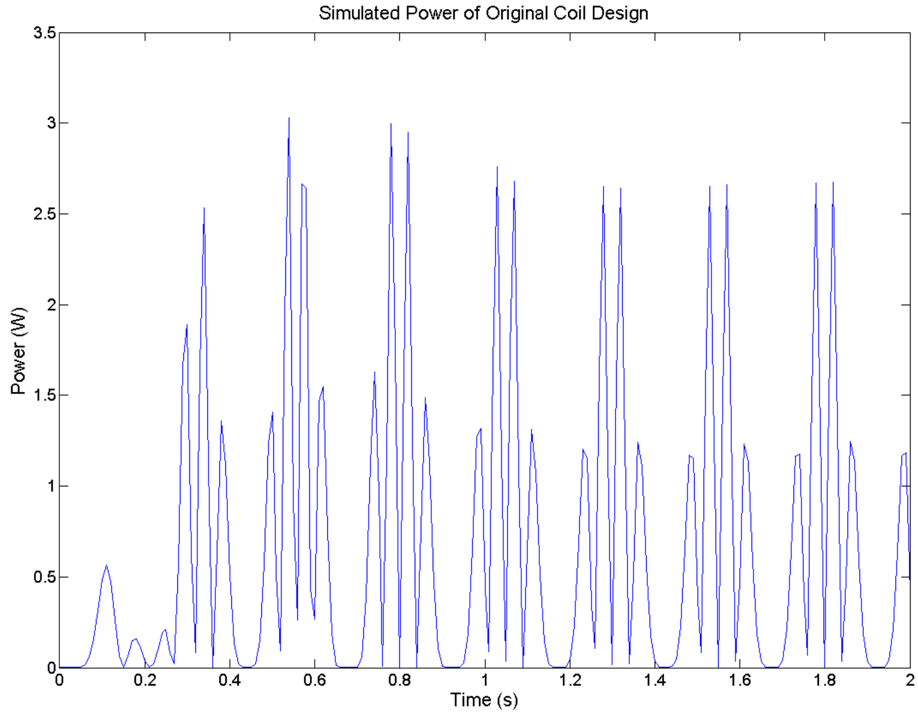

Figure 5.2: Simulated power of Stator A with respect to time

Figure 5.3 is a plot displaying the experimentally measured power generated by Stator A. The vertical axis shows the power measured across a 19Ω resistance. The timespan of the plot spans two seconds of the data collection process. At this point, the system is at steady state, illustrated by the similar amplitude of measured power magnitude. The peak power is approximately $0.17W$.

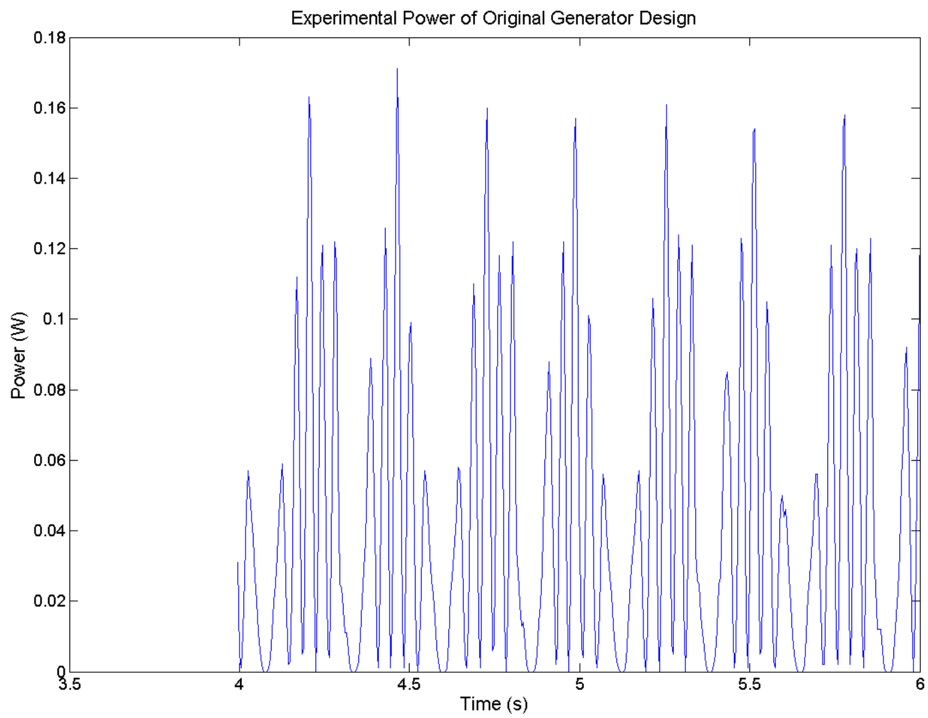

Figure 5.3: Measured power of Stator A over a two second time interval

When comparing the results from the simulation with the experimental results of Stator A, inconsistencies are detected in the magnitudes of generated power. The power predicted using Bateman's model has a peak power of $4.8W$ while the experimental has a peak power of $0.17W$. The error between the simulated power and experimental power is 2700%, indicating that something in the simulation was causing the power to be over predicted. An error of less than 15% is desirable, but the simulation would still be acceptable with an error of 20%. Two areas of the simulation were considered sources of inaccuracies. The inaccuracies come from the base excitation driven system of Bateman's model [14] and the magnetic flux approximation developed by Baker [15]. Adjustment to Bateman's model were made to eliminate the sources of inaccuracy. The inaccuracies of the model and the adjustments made to eliminate them are discuss further in Section 5.2.

5.2 Adjusting Simulink Model

5.2.1 Mechanical Simulation

The net force summation used to calculate the power within Simulink includes losses due to friction damping and deformation of a spring. The testing apparatus is directly driven by the motor, eliminating the friction and spring force components in the experimental apparatus. By eliminating the base excitation in the testing apparatus, a different system was created than the one that Bateman's model is predicting.

To adjust the simulation to accurately represent the test stand, the net force summation was eliminated and the translator position was modified to become the driving force of the simulation. Figure 5.4 shows a picture of the Simulink simulation after the spring and friction damping were eliminated. The original model was forced by the base acceleration of the system, and the adjusted model was forced by the position of the translator. The velocity was calculated by taking the derivative of the position. The velocity and position were then passed into the F_{mag} function to calculate the coupling force between the stator coil and magnetic translator. The MATLAB script uses an approximation of the magnetic field of the magnetic stator to calculate the coupling force between the translator and stator. The coupling force is then multiplied by the velocity to find the power that the generator is extracting from the system.

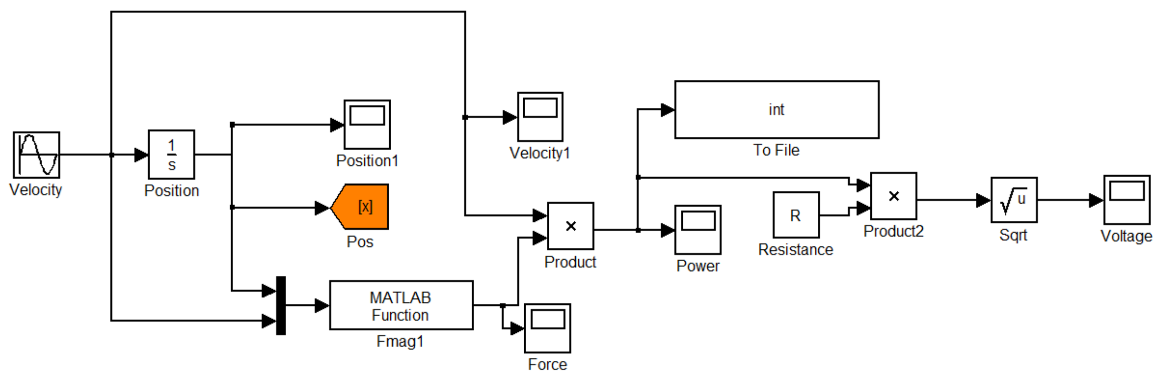

Figure 5.4: Modified Simulink simulation to reflect the physical changes in the testing apparatus

5.2.2 Magnetic Model

There is uncertainty in the magnetic field approximation because the entire magnetic field is approximated based on a calculated flux at the surface of the magnet. The magnetic field of a permanent magnet weakens exponentially with respect to distance from the magnet. By using a single point at the surface of the magnet to approximate the magnetic field experienced by the stator coils, the Simulink model was overestimating the magnitude of change in magnetic flux through the coils. This resulted in an overestimation of the induced current. The magnetic model is based on Baker's work as was discussed in Chapter 3. Along with the single-point approximation, Baker also presented an approximation of the weakening of the magnetic field as an exponential decay as shown in Equation 5.1 [15].

$$B_g = \hat{B}_g e^{-\frac{x}{l_g}} \tag{5.1}$$

To verify the accuracy of the magnetic field approximation, an AlaphLabs Inc. magnetometer was used to measure the maximum values of the magnetic field at various radial distances from the translator. The measured values were then compared to the value given by the MATLAB function used in the calculation of the coupling force. In order to get a good comparison, measurements of the experimental magnetic field were taken from $0cm$ to $3cm$ in $0.5cm$ increments.

Figure 5.5 displays a plot of the measured magnetic field. The vertical axis shows the maximum strength of the magnetic field and the horizontal axis displays the distance away from the magnetic translator in the radial direction. The amplitude of the magnetic field is given in Teslas and the distance is given in meters. The experimental magnetic field has a decay rate that appears to be exponential. The magnitude of the simulated field is $0.8751T$ while the average value of the experimental magnetic field is $0.1292T$, yielding a 577% error.

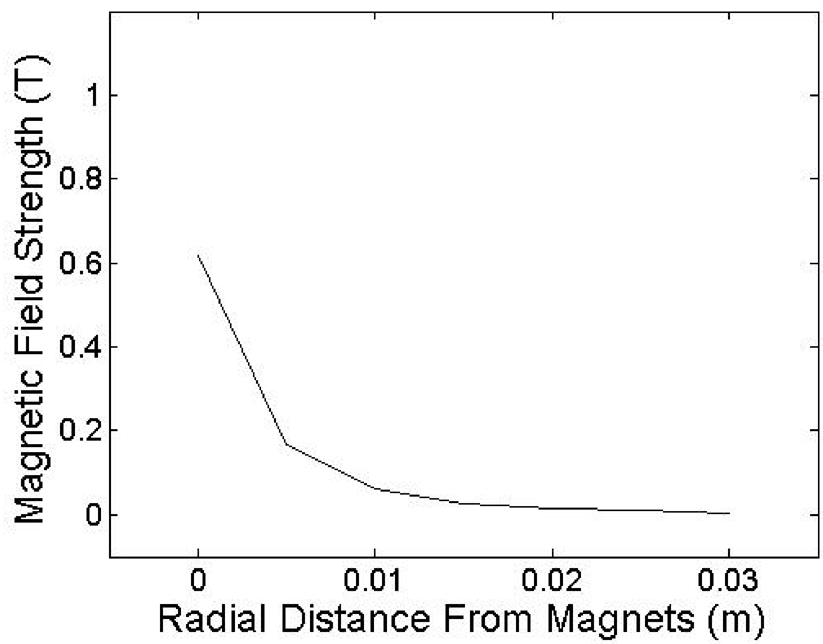

Figure 5.5: Experimental magnetic field strength as a function of radial distance away from magnetic stack

The error between the model and the experimental data is due to error within the assumptions made to develop the mathematical relationship. A calculated surface was used to approximate the average magnetic field experienced by the stator coils. The experimental data shows that the magnetic field decreases by approximately 50% at the outer edge of the stator coils. This indicates that using the value of magnetic field strength at the surface of the translator to approximate the field strength experienced by the stator coils is a poor assumption.

To obtain a more accurate prediction, the average magnetic field experienced by the stator coils should be used. Equation 5.1 approximates the decay of the magnetic field and is dependent on the field strength at the surface of the magnetic. Equation 3.3 gives an approximation of the surface field strength that is 41% larger than the measured field strength. In order to create an accurate prediction, the measured value of magnetic field strength at the surface of the translator was used in the calculation.

To include the decaying field strength within the simulation, a FOR loop was included in the MATLAB script file used to calculate the coupling force, which can be seen in B.2. The system of loop uses the decay rate given by Equation 5.1 and calculates the decayed magnetic field every $0.05mm$ in the a range from the inner edge of the stator coil to the outer edge of the stator coil. The average of the decaying field was then calculated and used in the prediction of the coupling force.

Figure 5.6 shows comparison between the simulated and measured magnetic field of the translator using the adjusted MATLAB function to approximate the magnetic field. The magnetic field is shown as the vertical axis and the radial distance away from the translator is shown on the horizontal axis. Both plots have the same value at the surface of the magnet because the experimentally measured value was used as the surface value in the function. The average percent error was 55.3% and the maximum percent error was 97.2%, as seen in the center of the plot. The 97.2% error occurs at $3cm$ above the surface of the magnets. The error is large at that point because both data points are approaching zero. While the error of the data is large, the difference between the two data points is $0.0048T$. With the simulation producing a magnetic field magnitude that differs on the scale of $.005T$, it can be assumed that the under estimation of the simulation will not cause significant error within the Simulink power simulation.

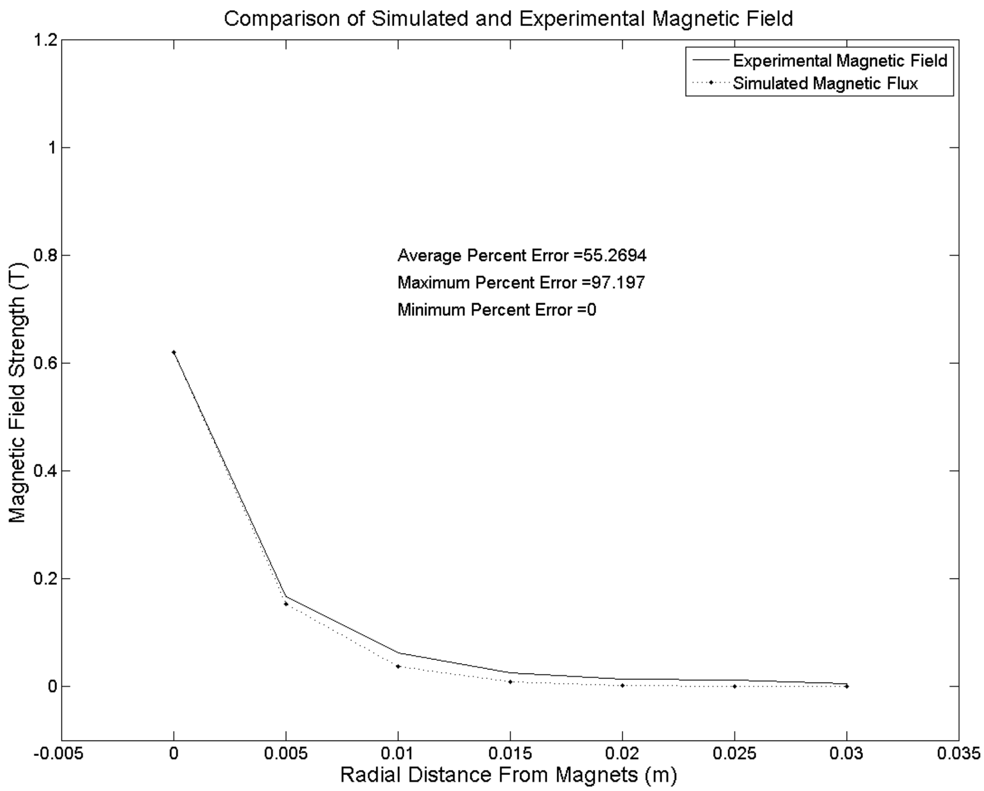

Figure 5.6: Comparison of experimental and simulated magnetic field strength as a function of distance away from the translator

Figure 5.7 displays a colormap plot of the approximated magnetic field strength as a function of the position along the translator shown on the horizontal axis in meters, and the position above the translator shown on the vertical axis in meters. The strength of the field is denoted by the color of the plot at each point. The magnitude of the magnetic field ranges from -0.62T to 0.62T. The field is mapped to approximately 2.25cm above the magnetic translator. Any distance farther than that can be considered approximately zero for the purposes of this research. The sign change of the field intensity is indicative of a pole change in the magnets. In the plot four full pole pairs are shown. A pole pair is made up of half of a magnet and half of a steel spacer. It can be seen that any distance beyond

$5mm$ has a significantly diminished magnetic field, therefore it produces little increase in power generation to have coils located beyond that distance.

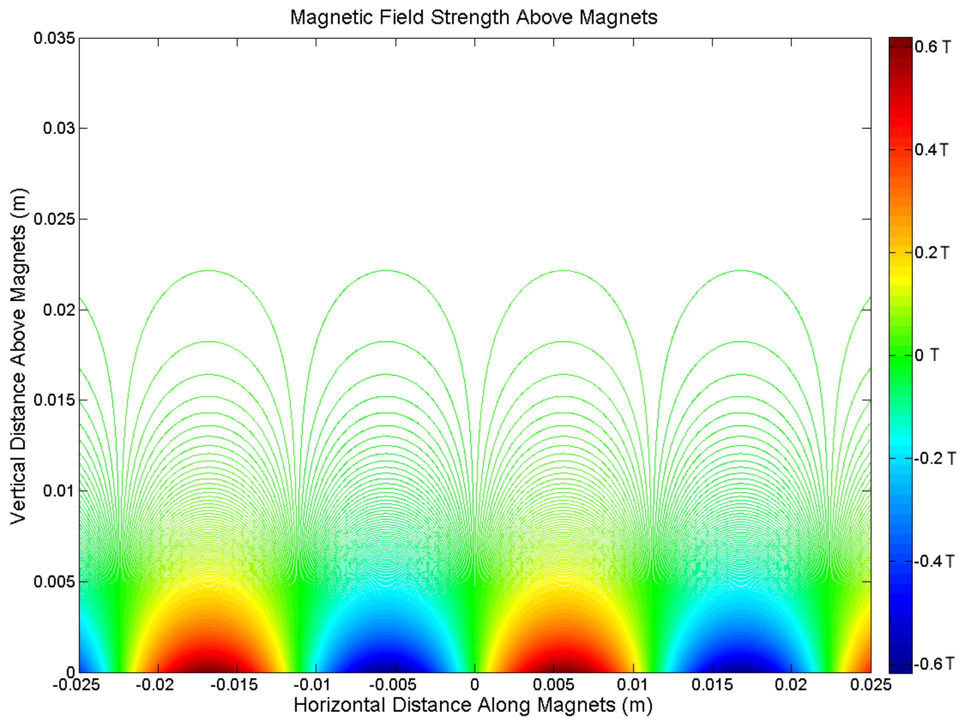

Figure 5.7: Colormap plot of the simulated intensity of the magnetic field as a function of position along and distance above magnetic translator

With the adjustments made to the model, it more accurately represented the testing apparatus. The new model will be referred to as the adjusted power model through the remainder of the document. The power and voltage of the experimental stators was measured and compared with the adjusted power model and is discussed in Section 5.3.

5.3 Testing with Adjusted Power Model

The adjusted power model was used to simulated the power generated by Stator A. The experimental results of Stator A were compared to the results from the adjusted power model. Figure 5.8 displays the power generation predicted for Stator A using an adjusted power model. The generated power is on the vertical axis and the time interval is displayed on the horizontal axis. The plot shows the power generated over a timespan of two seconds. The power generation peaks at $0.1867W$.

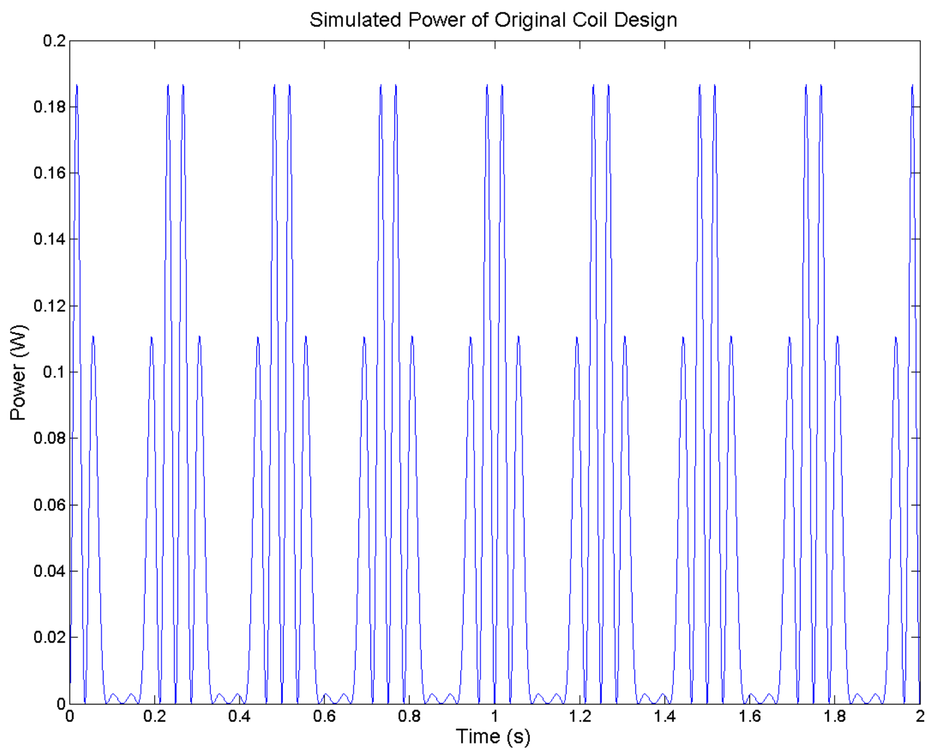

Figure 5.8: Simulated power of stator A using adjusted Simulink model

The power from the adjusted model is significantly lower than the results from Bateman's model [14]. The original model predicted a peak power generation of $4.8W$, whereas the adjusted model predicted a power of approximately $0.19W$. The peak experimental power generated was $0.176W$, indicating that the adjusted model is predicting a value closer to the actual value that is being generated. The percent error between the adjusted model and the experimental data is 6.1%. The desired error was presented to be 15% or less in Section 5.1. While the peak generation values were within an acceptable proximity to the experimental data, other parameters need to be predicted to validate the overall performance of the model. One thing that needed testing was whether or not the simulation was capturing the shape, frequency, and magnitude of each individual peak caused by the different pole pairs within the translator.

Figure 5.9 shows a detailed plot of the simulated and experimental power over the time period of approximately $0.3s$. The plot shows the power generated by the stator coil on the vertical axis and the time interval on the horizontal axis. The plot frames one half cycle of motion in the time range of $2.9s$ to $3.2s$ for the purpose of comparing the shape, frequency, and magnitude of each peak between the simulated and experimental data. The simulated data is shown with the black dashed line and the experimental data is shown with the blue solid line. The average percent difference between the data is 10.42% as can be seen near the top of the plot space.

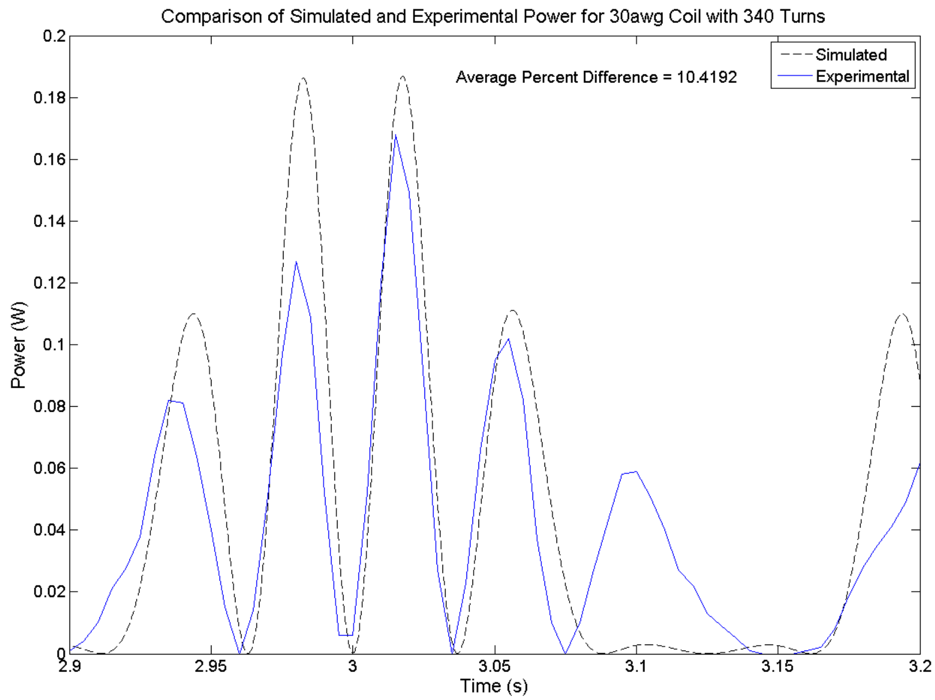

Figure 5.9: Comparison of generated power between the experimental data and adjusted Simulink model results using Stator A

Figure 5.10 displays a plot of a voltage comparison between the results of the adjusted power simulation and the experimentally measured data. The voltage is show as a function of time. One cycle of data is shown over the time interval of $2.9s$ to $3.15s$. The maximum voltages for experimental and simulated voltage are $1.79V$ and $1.88V$, respectively. The error in the maximum simulated voltage is 5.1% and the average error is 4.2%.

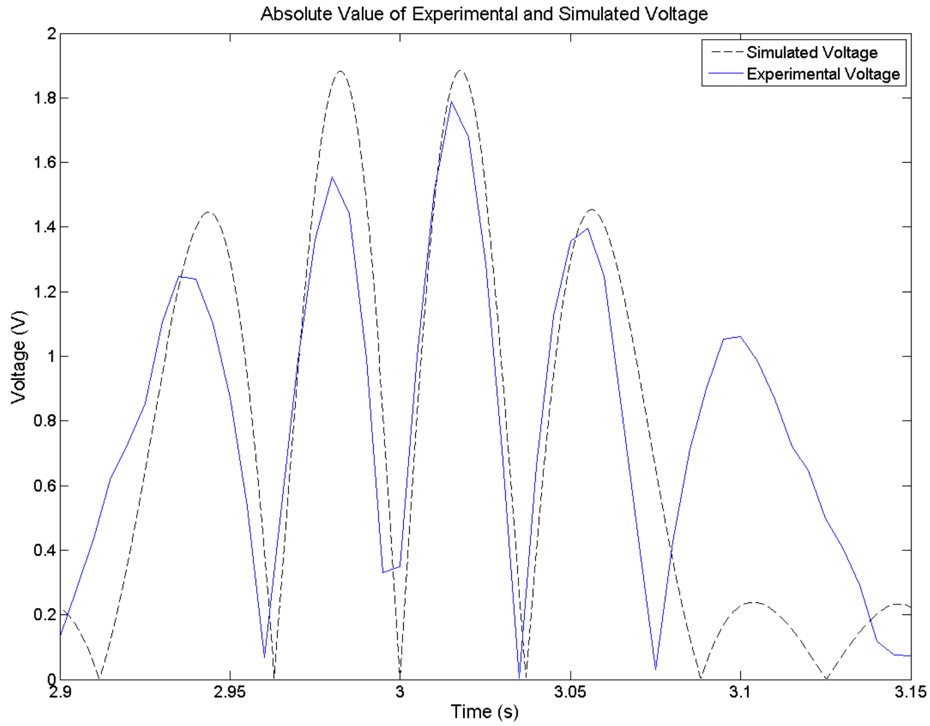

Figure 5.10: Comparison of simulated and experimental voltage generated by Stator A

Comparing the maximum power magnitudes gives an error of 9.9%, with a simulated value of $0.1869W$ and the experimental value of $0.1700W$. There are five peaks within the experimental signal and two are matched well, two are matched poorly, and one, the maximum peak, is matched at a 6.17% difference. Based on a comparison of the individual peak magnitudes, there is a $0.06W$ difference between the poorly matched peaks but as little as $0.005W$ at the well-matched peaks. The root mean squared(RMS) power was calculated to be $0.0437W$ for the experimental data and 0.0481 for the simulated data yielding a percent difference of 9.578%. The RMS power is significant because it is considered to be the usable power for AC power generation. While the simulation does not match each peak well, it captures the basic magnitude reasonable and estimates the RMS power within a desired accuracy.

The simulated data contains six peaks for every cycle of motion, while the experimental data contains five peaks. The difference is likely due to the beginning position of the translator with respect to the stator. The experimental apparatus likely begins the cycle of motion at the start of a magnetic pole pair, generating a large peak, then proceeding to stop at the end of a pole pair, passing through a total of five pole pairs. The simulated data starts and ends in the middle of a pole pair, generating two small peaks at the edges of the cycle. It also passes through five pole pairs, but has one pole pair split between the edges of the cycle of motion. In order to ensure this is causing the problem, the simulated translator needs to be shifted to start at the same point as the experimental apparatus.

The simulated data is held at a constant frequency of $2Hz$ while the experimental apparatus does not. The controller used set the frequency at $2Hz$ allows oscillations when running at steady state. To verify the model, the frequency is desired to be at a constant frequency of $2Hz$. The maximum percent difference in the frequency of the simulated and experimental data is 17%, which is still considered acceptable. The average frequency of the experimental data is $2.0Hz$, yielding an error of 0% when compared to the adjusted power simulation frequency.

The shape of the power signal was captured well as seen in Figure 5.9. The magnitude and frequency of the peaks is somewhat inaccurate, but the overall shape and size of the predicted power is reasonably predicted by the Simulink model. The model is intended to predict the instantaneous power of the system to a degree that gives an accurate estimate of the actual power that a generator of that size will produce. The model has been proven to predict the power generation of the generator made with 30awg magnet wire, with 480 windings, and a width of $1.2cm$

5.4 Further Testing with Various Generators

In order to ensure the adjusted power model worked for dissimilar stator designs, various stator were geometries needed. Three other generators were developed for this purpose as shown in Chapter 4. The three generators have varying coil widths, heights, wire diameter, number of windings, and resistances. The possibility exists that the Simulink model only works within a small range of parameters and it is important to know the limits of the model to avoid using results that may not be accurate. Figure 5.11 displays a picture of the four generators that were designed and experimentally tested to verify the accuracy of the Simulink model. From left to right, the picture displays Stator D, Stator C, Stator B, and Stator A.

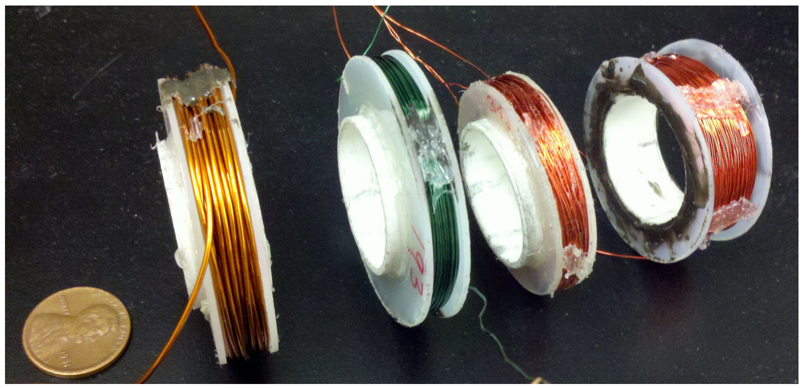

Figure 5.11: Four stator coils designed, fabricated, and tested for the purpose of verifying the power prediction of the adjusted Simulink model

5.4.1 Results for All Stator Designs

The power data, from the four stators was measured and is presented in Table 5.1. Comparisons were made between the maximum generated power values and the average generated power values. The error between the adjusted power model and the experimentally measured data is shown in the two rightmost columns. The largest error in the maximum power magnitudes was 28.8%, which occurred when comparing values of Stator C. The largest error of the average power was 10.4%, from the comparison of Stator A. The max value error of Stator C is the only point that does not have an error smaller than the desired 15%. While the peak value of generated power for Stator C was not accurately predicted by the adjusted power model, the average power was predicted to within 4.9%.

The model successfully predicted average power generation for the four stators tested. The maximum power generated was $0.17W$ from Stator A.

Table 5.1: Power results from four experimental stators

Stator Name and Data Type		Max Power(W)	Mean Power(W)	Max Value Error	Mean Value Error
Stator A	Simulated	0.187	0.048	9.9%	10.4%
	Experimental	0.17	0.044		
Stator B	Simulated	0.109	0.028	10.0%	0.9%
	Experimental	0.099	0.028		
Stator C	Simulated	0.095	0.024	28.8%	4.9%
	Experimental	0.133	0.023		
Stator D	Simulated	0.043	0.011	7.3%	1.3%
	Experimental	0.046	0.011		

Results and comparison of the voltage data are shown in Table 5.2. The voltage is significant when designing a method to rectify the current. The average voltage was successfully predicted by the adjusted power model having a maximum error of 19.2% when simulating Stator D. The maximum peaks were predicted to within 16.4% for the four stators tested. Stator A generated the largest voltage at $1.79V$. The smallest generated voltage was 0.17V from Stator D.

Table 5.2: Voltage results from four experimental stators

Stator Name and Data Type		Max Voltage(V)	Mean Voltage(V)	Max Value Error	Mean Value Error
Stator A	Simulated	1.88	0.75	5.2%	4.2%
	Experimental	1.79	0.79		
Stator B	Simulated	1.28	0.51	1.4%	10.9%
	Experimental	1.26	0.57		
Stator C	Simulated	0.57	0.22	16.4%	8.5%
	Experimental	0.68	0.25		
Stator D	Simulated	0.15	0.06	13.6%	19.2%
	Experimental	0.17	0.07		

The frequency was tested to ensure that the model was accurately representing the experimental apparatus. Due to the steady-state oscillations of the experimental apparatus, it was unclear if a constant simulation frequency was practical. The largest error in the frequency was 11.9% when testing Stator D, indicating that setting a constant $2Hz$ for the simulation is acceptable. The average frequency of the testing apparatus was maintained within $< 1\%$ of the desired value of $2Hz$.

Table 5.3: Frequency results from four experimental stators

Stator Name and Data Type		Max Frequency(Hz)	Mean Frequency(Hz)	Max Value Error	Mean Value Error
Stator A	Simulated	2	2	11.4%	0.0%
	Experimental	2.5	2.0		
Stator B	Simulated	2	2	10.3%	0.1%
	Experimental	2.2	2.0		
Stator C	Simulated	2	2	11.0%	0.1%
	Experimental	2.2	2.0		
Stator D	Simulated	2	2	11.9%	0.0%
	Experimental	2.2	2.0		

After analysing the results, it was determined that the adjusted power model was able to accurately predict the average values of power and voltage to within 20% of the experimental data. The peak predicted power was not within 20% of the experimental for Stator C. This could be due to an inaccurate measurement of device geometry. The model was found to be sensitive to coil width and height inputs. Due the uneven surface of the wound wire, it was difficult to accurately measure the width and height, which could have affected the simulation accuracy. The voltage predictions, for peak and average, were all within 20% of the measured values, indicating that the adjusted power model was accurate when predicting voltage.

5.5 Comparison of Experimental and Simulated Data Over a Range of Frequencies

The frequency range of a person walking is $1.7Hz - 2.3Hz$, as was discussed in Chapter 2 [9, 17]. In order to ensure the simulation predicts the average power generation accurately for all frequencies in this range, data was taken from all four generators starting at a frequency of $1.5Hz$ and increasing by $0.1Hz$ to $2.5Hz$. Simulations were performed on the four stators for the range frequencies to obtain a comparison between the simulated and experimental data. The RMS and Average generated power values were compared.

Figure 5.12 is a plot that displays the average power generated from the four stator coils over a frequency range of $1.5Hz - 2.5Hz$. The vertical axis displays the average power generated and the horizontal axis displays the frequency of motion. The experimental data is denoted with blue markers and the simulated data is denoted with red markers. The legend show the marker types of each data set. The legend is located on the right edge of the plot near the top. In the top-left corner of the plot area, the error of all of the averaged values is printed. The errors of Stator A ,B, C, and D were: 13.23%, 0.82%, 6.09%, and 11.27%, respectively. The error displayed is an average over the range of frequencies.

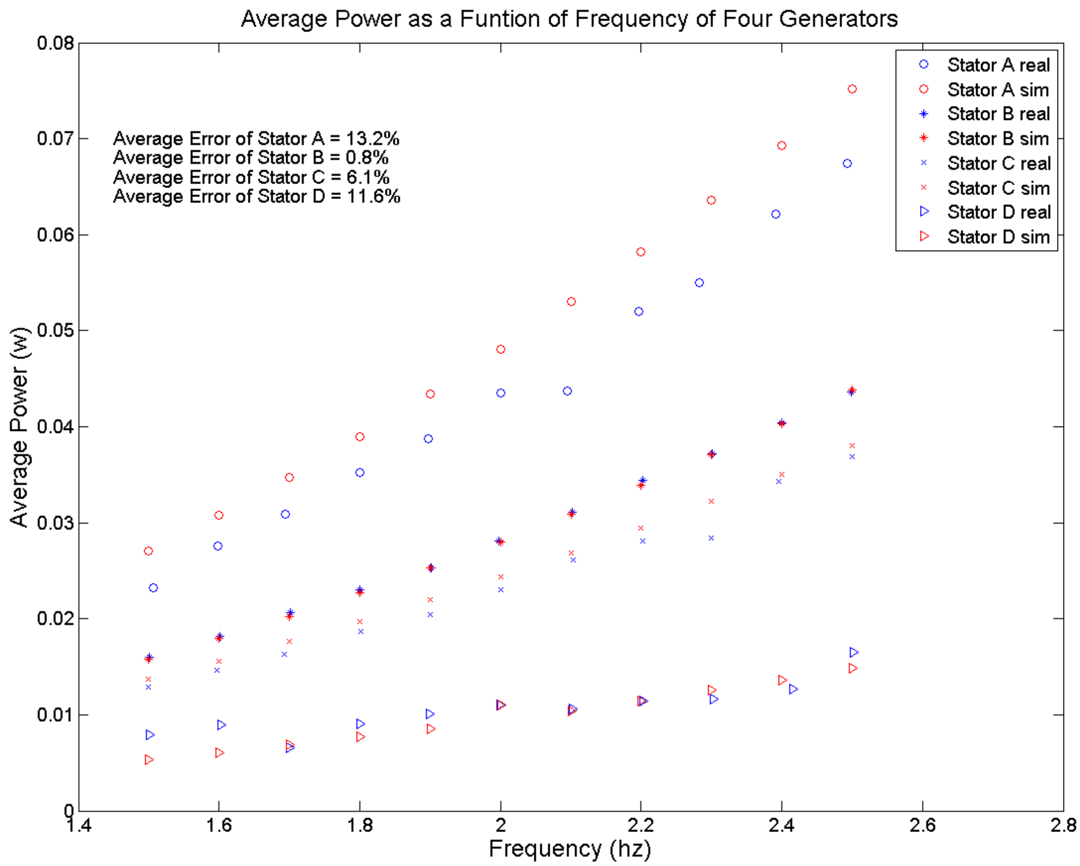

Figure 5.12: Plot of average power as a function of frequency of the four test generators

It can be seen in Figure 5.12 that simulations of Stator B produced the smallest error in the average generated power. The predicted power of Stator A has an error of 13.2%, which is the largest of the four stators. The curves all appear to have a linear trend with frequency over the given frequency range. The Stator A appears to have the steepest slope while Stator D has the smallest slope. The results of the average power indicates that the generator is accurate over the entire range of frequencies that the backpack will be expected to work in. The largest error is under the desired value of 15% error.

The plot shown in Figure 5.13 displays the RMS power of the generators as a function of frequency. Plots of the simulated and experimental RMS power generated by the four stators are plotted on a single graph. The experimental data is denoted with blue markers and the simulated data is denoted with red markers. The generated power is shown on the vertical axis and the frequency on the horizontal axis. The legend is located near the top of the plot on the right side. Near the top of the plot on the left side, the error of the predicted power of the four stators is displayed. The errors in the predicted RMS power of Stator A, B, C, and D are as follows: 12.47%, 7.90%, 2.41%, and 26.76%. The smallest error is seen in the prediction of Stator C. The largest error is seen in the prediction of Stator D.

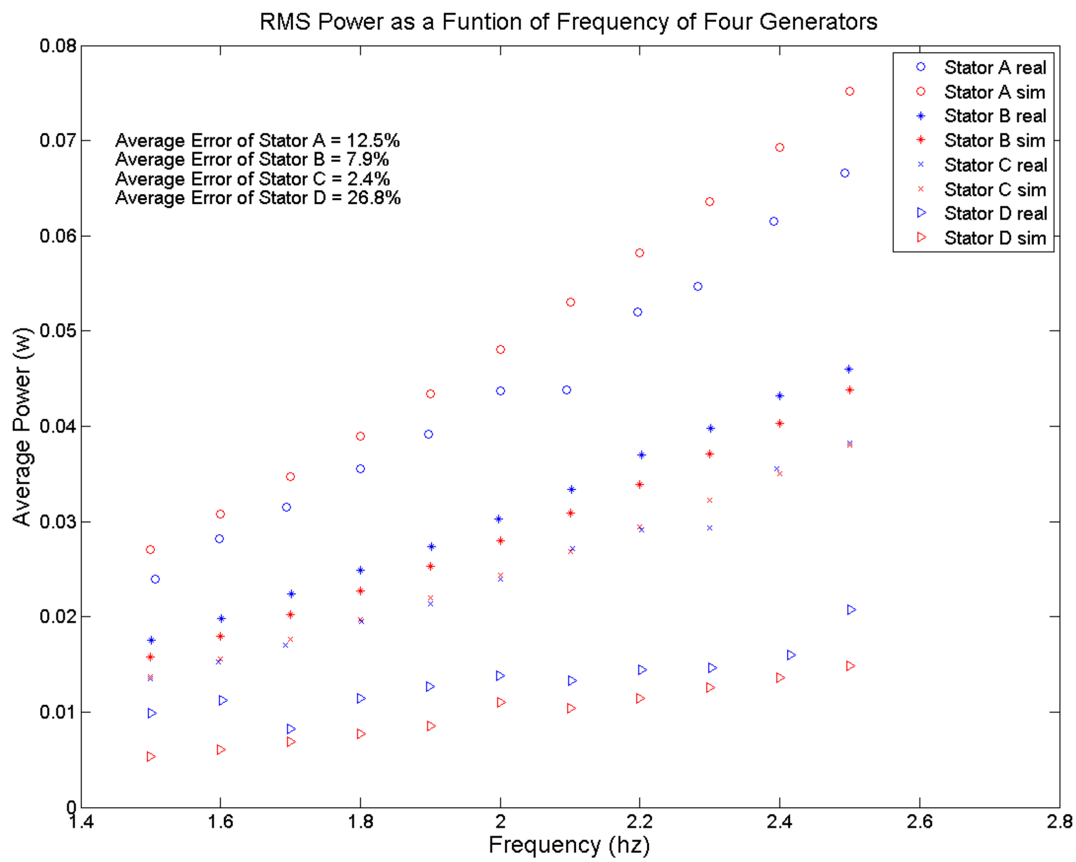

Figure 5.13: Plot of RMS power as a function of frequency for the four experimental generators

The curves appear to have an increasing slope as the frequency increases, indicating a polynomial or exponential relationship between the power and frequency. It is likely that the relationship is a power curve, but most of the generators appear to be linear because of the small region of frequency that is shown.

The errors of Stators A, B, and C are acceptable but Stator D displayed a 26.76% error of the predicted RMS power. It can be seen in Figure 5.13 that the first two experimental data points of Stator D are significantly higher than the power generated at larger frequencies. The power should follow an increasing trend with increasing frequency. The data points at frequencies of $1.5Hz$ and $1.6Hz$ are likely due to some inconsistency in the experimental apparatus and are not indicative of a maximum power frequency at those points. The comparison of Stator D needs to be performed again before conclusions can be drawn.

5.6 Concluding Results

When looking at the error in the comparisons of the four experimental stators, it was shown the most error was indicated on the Stators A and D. These devices have larger coil widths than did the other two devices. When the coil width is large, at transitions between magnetic poles, coils at either side of the device will experience magnetic fields with opposing polarities. When the flux of the opposing fields changes, causing current to be induced in the generator, the induced current will flow in opposite directions. The opposing current will cancel out, causing zero net power generation through the device. This phenomena is likely the cause of the larger error experienced when modelling stators with larger coil widths because the simulation does not account for opposing current flow. When calculating the power, the absolute value is used, which forces the current to be positive. The width of the generators should be kept at approximately the width of the magnets in order to minimize the amount of error in the simulation.

The direction of the magnetic field would need to be accounted for as a first step to approximating the cancellation of current due to opposing magnetic fields. The position of the stator windings would then need to be indexed to determine what direction of field each of the windings is experiencing. Currently, the stator position is based on a single point in the center of the width of the stator, which would not indicate if the windings at either edge of the stator experiencing opposing magnetic flux.

The average generated power of the experimental inductive generators was predicted with an error of less than 15%, indicating that the model was valid and should be used to determine an optimum stator size. In order to find the optimum size, a MATLAB script was written to vary coil width, coil height, and wire size of the stator, and run power simulations on the various configurations. The configuration to produce the largest average power generation was considered the optimum design for the backpack generator. The results of the optimization script are discussed in Chapter 6.

CHAPTER 6

CONCLUSIONS AND FUTURE WORK

The goal of this thesis was to experimentally validate the simulation developed by Bateman. The first step in this process consisted of designing and fabricating a testing apparatus and linear permanent magnet generators. With a working experimental apparatus, comparisons were made between the simulated power generation and the experimental power generation. It was shown that the simulation was over predicting the power generation of the experimental data. To correct the simulation, adjustments were made to the magnetic field model to ensure that it was predicting a realistic magnetic flux through the stator coils. Power generation results from the modified simulation and the experimental apparatus were compared to determine the accuracy of the model. The comparisons displayed that the modified simulation was valid because it had an accuracy exceeding 80%. After the validation process was completed, the simulation was then used to predict an optimal generator design, which is presented in Section 6.1.

6.1 Using Simulink Model to Predict the Optimal Generator Design

In Chapter 5, various comparisons between the experimental and simulated power of four generators were done. These comparisons showed that the simulation was accurate at predicting the average power generation of an air-cored linear inductive permanent magnet generator. The simulation data was considered acceptable if it predicted the power to within 20% of the experimental data. Through the comparisons, it was shown that the average simulated power never exceeded a 13% difference for any of the devices over a range of frequencies from $1.5Hz - 2.5Hz$. On Stators B, and C, which had a coil widths smaller than the magnet width, the error was smaller than 10%. This led to the conclusion that the model does not predict losses due to opposing current induction within the generator. Opposing current is induced when the windings from a generator experience changing magnetic flux in opposite directions simultaneously.

The results showed a significant increase in power generation in the generators made with smaller diameter magnet wire. The largest average power was produced by the two coils that were wound with 30awg magnet wire. The generators with smaller diameter wire contain more windings of those with the larger diameter, but also have more internal resistance. Voltage is proportional to the number of winding in the stator. Smaller diameter wire allows for more windings in a given area, but also increases the internal resistance of the stator. If the diameter of the wire were continually decreased, a point would be reached where the internal resistance would get large enough to hinder power generation.

Because the model was proven to predict power generation in the proposed system, it was used to estimate the optimal design for a linear permanent magnet generator to integrate into a suspended load, energy scavenging backpack. The main properties of concern when designing the generator were considered to be the coil width, coil height, and the diameter of wire to be used. These are all constraints that are directly set by the designer, and have a large impact on the generation of the device. Some parameters of concern that were not directly set in the optimization process were: number of coil windings, packing factor of the wire, and resistance of the generator. These values were dependent on the type of wire used and the fabrication process. The packing factor was set to an assumed value of 0.6. The value was chosen as a desired packing factor with an improved fabrication process based on Gogue and Stupak [28]. The packing factor is important to how much power the device will produce, but is dependent on the fabrication process, and the size of wire used. The number of wire windings is set by the packing factor of the wire and the area that the windings are contained within. This value was calculated within the simulation during the optimization process. Similarly, the resistance of the generator was calculated by the simulation based on geometric properties of the device. Resistance of copper wire is a function of the diameter and length of wire used. Values for the diameter and resistance per unit length of copper magnet wire were given by Superior Essex and are shown in Table 6.1 [29].

Table 6.1: Resistance and diameter of various gauges of magnet wire [29]

Wire Gauge	Resistance (Ω/m)	Wire Diameter (m)
38	2.127	0.102E-3
36	1.361	0.127E-3
34	0.8573	0.160E-3
32	0.5316	0.203E-3
30	0.3403	0.254E-3
28	0.2143	0.320E-3
26	0.1346	0.404E-3
24	0.08822	0.511E-3

The wire sizes shown in Table 6.1 were chosen as inputs in the optimization script. A MATLAB script was written to vary the coil width and height in the given range with a step size of $0.2mm$. The MATLAB script opened and ran the adjusted power model for each of the width and height dimensions while using all of the wire sizes displayed in Table 6.1. The dimensions for the coil width parameter was set to a maximum of $12mm$ with a minimum of $1mm$. The program gets unstable as the coil width gets larger, but it was shown to be within approximately 13% accuracy for Stator A, which had a $12mm$ width. The coil height was given a minimum of $1mm$ and a maximum of $10mm$. Any distance larger than $10mm$ away from the magnets has a significantly diminished magnetic field strength and would not produce enough current to offset the added resistance. The Simulink simulation was then adjusted to take the three parameters as inputs into the magnetic force function developed by Bateman [14]. The step size for the coil width and height ranges were set to $0.2mm$. The optimization program tested 20608 variations of stator geometry. The optimum design in this range was found to be a generator using 32awg magnet wire with a coil width of $12mm$ and a coil height of $2.2mm$, which could produce an average power of $0.30W$. The generators with the 32awg wire were found to produce the most power at every coil width and height.

Figure 6.1 shows a surface plot of the average power simulated for the generator made with 32awg wire. The vertical axis shows the average power in Watts, the left-facing axis shows the coil width in meters, and the right-facing axis shows the coil height in meters. The color bar indicates the magnitude of generated power in Watts. Dark blue indicates low values of power generation and dark red indicates the highest values of power generation. Optimum power is shown by the peak value on the plot at a coil height of $0.0022m$ and a coil width of $0.012m$. When looking at the plot as a function of winding height, the power generation can be seen to increase quickly from $0.001m$ through $0.0022m$, then it gradually decreases, due to the decreasing magnetic field. When looking at power generation as a function of winding width, it can be seen to increase gradually through the whole range of values from $0.001m - 0.012m$.

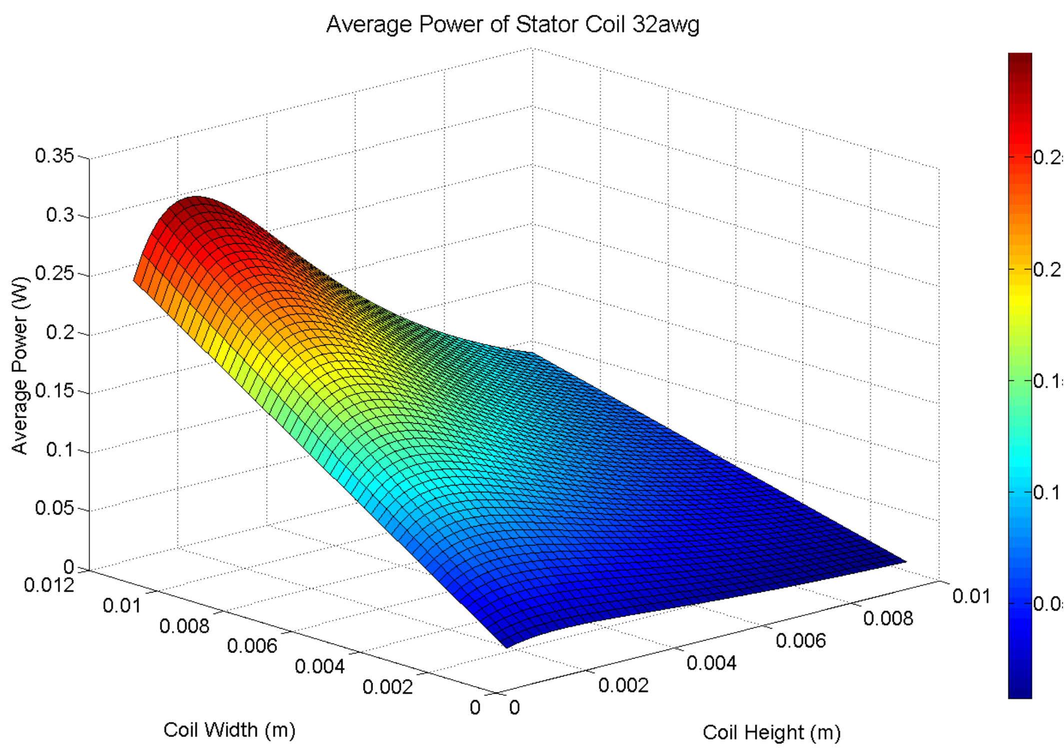

Figure 6.1: Surface plot displaying the power output of a simulated generator with 32awg wire

The results from the figure indicate that the distance the coils are located away from the magnetic stack is crucial to finding the maximum power generation. The peak distance located within a small area, and the power generation decreases rapidly with small or larger values. A precise fabrication technique is needed to ensure the height of the coils falls within this range. The current fabrication method creates an uneven packing of the wire, causing a non-uniform height of the windings. A mechanism needs to be implemented to place the wire at a specific pitch to ensure tight packing of the wire, as well as a uniform surface height of the outer-most wires.

In order to get the best coil possible, the scope of width and height should be narrowed to within one square millimetre of the optimum generator presented in this section. The step size should be lowered in this range to provide more resolution around the area of importance. This would produce a more precise value for the optimum height and width of the windings. The gauges of wire should also be narrowed down to pick the optimum wire diameter. The current simulation ran with increments of every 2 gauges of wire. This should be resolved into half gauges of wire encompassing up to 34awg and down to 30awg sizes. Using the simulation with the highly resolved parameters would yield a design that ensures the most possible generation based on the current system.

6.2 Future Work

The next step of the project should be implementing the parameter refinements proposed in the Section 6.1 to find the optimal wire size and stator size for the given translator. A working prototype then needs to be built and refined using techniques to ensure tight even packing of the wire on the generator. This would provide a better packing factor, allowing more windings to fit into a smaller area. The optimization was based on a packing factor of 0.6, which is a desired value based on Gogue and Stupak's work [28].

After a prototype of the proposed optimal design is fabricated, the model optimization needs to be tested for accuracy. Once verified, the stator should to be built in LTCC to ensure protection from the environment, electrical interference, and physical wear. The electrical traces should be a proper width to give a resistance approximately equal to that of the 32awg wire. The spacing of the traces will need to be calculated to provide at least a 0.7 packing factor. It should contain the proper number of layers to equal $0.012m$ and have an outer diameter of $0.0022m$. These coils should be developed in a modular, so that stator can be added or subtracted for greater power generation potential.

Along with a generator made of LTCC, a rectification process will need to be developed to convert the alternating current coming out of the generator to direct current. The electricity will be stored in small on-board batteries that can be directly plugged into charge ports on various electronic equipment. By storing the electricity in the battery, a steady power and voltage are guaranteed to be supplied to the device and electricity is not wasted when no devices are connected.

The last phase of the project will be to design and fabricate a backpack frame that will house the generators and magnetic translator within the frame. Springs will need to be sized and attached to ensure a proper phase shift of the movement of the pack load with respect to the person. Ideally, the frame will contain rectifying circuit and batteries as well as the generators to ensure that space in the backpack is taken by the device.

REFERENCES

[1] J. Fjelstad and P. John Murray, "Bringing wireless to the battlefield," *RF Design*, pp. 48–56, April 2001.

[2] P. Patel-Predd, "Traveling light," *IEEE Spectrum*, pp. 20–21, July 2006.

[3] P. M. Quesada, L. J. Mengelkoch, R. C. Hale, and S. R. Simon, "Biomechanical and metabolic effects of varying backpack loading on simulated marching," *Ergonomics*, vol. 43, no. 3, pp. 293–309, 2000.

[4] N. R. C. Committee on Electric Power for the Dismounted Soldier, *Energy-Efficient Technologies for the Dismounted Soldier*. The National Academies Press, 1997.

[5] D. Dunn-Rankin, E. Leal, and D. Walther, "Personal power systems," *Progress in Energy and Combustion Science*, vol. 31, no. 5, pp. 422–465, 2005.

[6] J. Xu, K. Vanderlick, and D. A. LaVan, "Energy conversion in protocells with natural nanoconductors," *International Journal of Photoenergy*, vol. 2012, 2012.

[7] J. Feenstra, J. Granstrom, and H. Sodano, "Energy harvesting through a backpack employing a mechanically amplified piezoelectric stack," *Mechanical Systems and Signal Processing*, vol. 22, no. 3, pp. 721 – 734, 2008.

[8] N. Shenck and J. Paradiso, "Energy scavenging with shoe-mounted piezoelectrics," *Micro, IEEE*, vol. 21, pp. 30 –42, may/jun 2001.

[9] L. C. Rome, L. Flynn, E. M. Goldman, and T. D. Yoo, "Generating electricity while walking with loads," *Science*, vol. 309, no. 5741, pp. 1725–1728, 2005.

[10] N. Baker, M. Mueller, and E. Spooner, "Permanent magnet air-cored tubular linear generator for marine energy converters," in *Power Electronics, Machines and Drives, 2004. (PEMD 2004). Second International Conference on (Conf. Publ. No. 498)*, vol. 2, pp. 862 – 867 Vol.2, march-2 april 2004.

[11] O. Danielsson, M. Leijon, and E. Sjostedt, "Detailed study of the magnetic circuit in a longitudinal flux permanent-magnet synchronous linear generator," *Magnetics, IEEE Transactions on*, vol. 41, pp. 2490 – 2495, sept. 2005.

[12] L. Szabo, C. Oprea, l.-A. Viorel, and K. Biro, “Novel permanent magnet tubular linear generator for wave energy converters,” in *Electric Machines Drives Conference, 2007. IEMDC ’07. IEEE International*, vol. 2, pp. 983 –987, may 2007.

[13] O. Danielsson, *Wave Energy Conversion : Linear Synchronous Permanent Magnet Generator*. PhD thesis, Uppsala University, Division for Electricity and Lightning Research, 2006.

[14] H. A. Bateman, “Linear electromagnetic energy scavenging device designed in low temperatrue co-fired ceramics,” Master’s thesis, Boise State University, 2011.

[15] J. N. Baker, *Linear Generators for Direct Drive Marin Renewable Energy Converters*. Theis(ph.d), University of Durham, 2003.

[16] J. B. D. M. Saunders, V. T. Inman, and H. D. Eberhart, “The major determinants in normal and pathological gait,” *The Journal of Bone & Joint Surgery*, vol. 35, no. 3, pp. 543–558, 1953.

[17] A. V. Rowlands, M. R. Stone, and R. G. Eston, “Influence of speed and step frequency during walking and running on motion sensor output,” *Medicine and Science in Sports and Exercise*, vol. 39, no. 4, pp. 716–727, 2007.

[18] S. A. Gard, S. C. Miff, and A. D. Kuo, “Comparison of kinematic and kinetic methods for computing the vertical motion of the body center of mass during walking,” *Human Movement Science*, vol. 22, no. 6, pp. 597 – 610, 2004.

[19] I. Ivanova, O. Agren, H. Bernhoff, and M. Leijon, “Simulation of wave-energy converter with octagonal linear generator,” *Oceanic Engineering, IEEE Journal of*, vol. 30, pp. 619 –629, july 2005.

[20] I. Ivanova, O. Agren, H. Bernhoff, and M. Leijon, “Simulation of cogging in a 100 kw permanent magnet octagonal linear generator for ocean wave conversion,” in *Underwater Technology, 2004. UT ’04. 2004 International Symposium on*, pp. 345 –348, april 2004.

[21] J. Wang, W. Wang, G. W. Jewell, and D. Howe, “Design of a miniature permanent-magnet generator and energy storage system,” *Industrial Electronics, IEEE Transactions on*, vol. 52, no. 5, pp. 1383–1390, 2005.

[22] N. Baker and M. Mueller, “A low speed reciprocating permanent magnet generator for direct drive wave energy converters,” in *Power Electronics, Machines and Drives, 2002. International Conference on (Conf. Publ. No. 487)*, pp. 468 – 473, june 2002.

[23] O. Danielsson, K. Thorburn, M. Eriksson, and L. Mats., “Permanent magnet fixation concepts for linear generator,” in *Fifth European wave energy conference*, sept. 2003.

[24] E.I. DuPont de Nemours and Company, *951 Green Tape*, 2001. MCM951 datasheet.

[25] D. Plumlee, J. Steciak, and A. Moll, “Development of a micro-nozzle and ion mobility spectrometer in ltcc,” in *Microelectronics and Electron Devices, 2004 IEEE Workshop on*, pp. 95 – 98, 2004.

[26] J. Stewart, *Calculus, 6E: Custom Edition for Vanderbilt University.* Cengage Learning, 2008.

[27] A. R. Hambley, *Electrical Engineering Principles and Applications.* New Jersey, USA: Prentice Hall, third ed., 2004.

[28] G. P. Gogue and J. Hoseph J. Stupak, *Theory and Practive of Electromagnetic Design of DC Motors and Actuators.* Oregon, USA: G2 Consulting.

[29] SUPERIOR ESSEX, *magnet wire/winding wire engineering data handbook*, 1st ed., December 2009.

APPENDIX A

LABVIEW VI

A.1 LabVIEW Front Panel

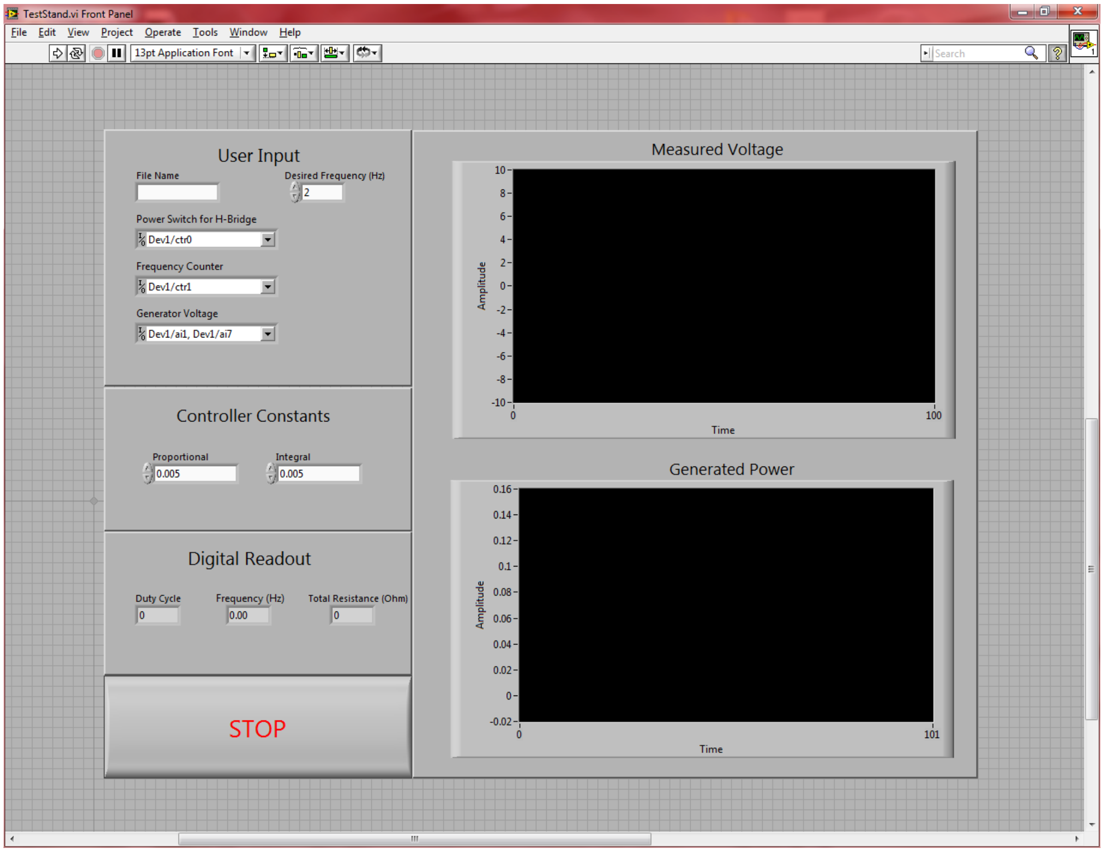

Figure A.1: Front panel of LabVIEW program used to control, and collect data from testing apparatus

A.2 LabVIEW Block Diagram

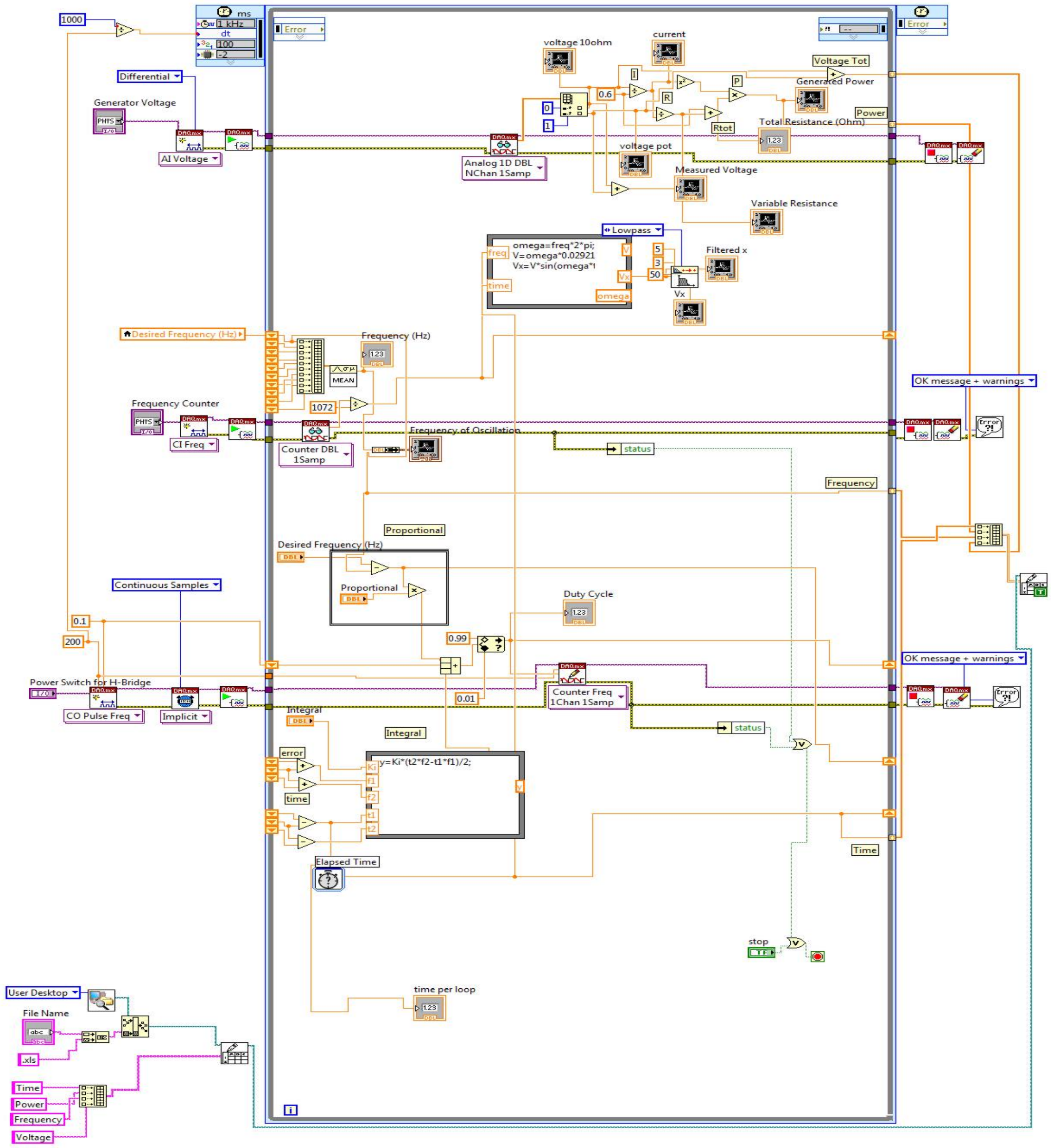

Figure A.2: LabVIEW program used to control, and collect data from testing apparatus

APPENDIX B

MATLAB SCRIPTS

B.1 Simulation Parameters

```
clear
close all
K = 8000; %N/m 8000
C = 189.315; %kg/s 189.315
M = 1.67; %kg (61lb) 28 %%new 1.670kg
Y = 0.025; %m (0.984in) .025
w = 12.566; %rad/s (2hz) 12.566
A = Y*w^2; %m/s^2
N = 1;     %number of generators
R = N*019;   %Resistance of the system
```

B.2 Magnetic Force Approximation

```
function Baave = Fmag1_30g_340tmod2(u)
%Inputs
%u(1)= relative position
%u(2)= relative velocity
v = u(2);
x = u(1);
%%
%Constants
gap = 0.0002;                %Air gap (m)
ch = 0.00665;                %Coil thickness (m) =0.0052
Rm = 0.0127;                 %Magnet Radius (m)
wm = 0.0056;                 %Magnet Width (m)
Wp = 2*wm;                   %Pitch of magnet and spacer (m)
ws = wm;                     %Steel Spacer Width (m)
cw = .0056;                  %Coil Width (m) =Wp
lg = Wp/pi;                  %Effective Air Gap
Bgh = 0.6200;                %Measured Surface Flux Density (T)
Ro = Rm + gap +ch;           %Outer Radius of coil (m)
Ri = Rm + gap;               %Inner Radius of coil (m)
vol = pi*cw*(Ro^2-Ri^2);     %Volume of Coil (m)
ra = (Ri + Ro)/2;            %Average Radius of coil (m)
Ncoil = 340;                 %Number of Coils =480
Ndevices = 1;                %Number of Devices
Lp = Ndevices*Ncoil*2*pi*ra; %Path length of coil
Rsis = 15;                   %Resistance of Coil (ohms)=10
%%
```

```
%Calculate flux density along rotor (T)
step = .00005;
i = 1;
Basum = zeros(1,(Ri:step:Ro));
for h = gap:step:gap+ch
    Bg = Bgh*exp(-h/lg);
    if 0 < x && x < Wp
        Ba = Bg*sin(pi*x/Wp);
    elseif Wp < x && x < 2*Wp
        Ba = -Bg*sin(pi*x/Wp);
    elseif 2*Wp < x && x < 3*Wp
        Ba = Bg*sin(pi*x/Wp);
    elseif -Wp < x && x < 0;
        Ba = -Bg*sin(pi*x/Wp);
    elseif -2*Wp < x && x < -Wp;
        Ba = Bg*sin(pi*x/Wp);
    elseif -3*Wp < x && x < -2*Wp;
        Ba = -Bg*sin(pi*x/Wp);
    else
        Ba = 0;
    end
    Basum(i) = Ba;
    i=i+1;
end
Baave = mean(Basum);
%%
%magnetic force (N)
Fm = (cw*pi*v*Lp^2*Baave^2*lg*exp(-2*gap/lg)*(2*Ri+lg-(2*Ro+lg)...
```

```
*exp(-2*ch/lg)))/(2*Rsis*vol);
```

B.3 Magnetic Flux Comparison

```
clear all
close all
tic
%%
%Constants
gap = 0.0002;                 %Air gap (m)
ch = 0.00665;                 %Coil thickness (m) =0.0052
Rm = 0.0127;                  %Magnet Radius (m)
wm = 0.0056;                  %Magnet Width (m)
Wp = 2*wm;                    %Pitch of magnet and spacer (m)
ws = wm;                      %Steel Spacer Width (m)
mur = .99998;                 %Permeability
cw = .0056;                   %Coil Width (m) =Wp
lg = Wp/pi;                   %Effective Air Gap
Bgh=0.6200;                   %Flux Density at surface of Rotor (T)
Ro = Rm + gap +ch;            %Outer Radius of coil (m)
Ri = Rm + gap;                %Inner Radius of coil (m)
vol = pi*cw*(Ro^2-Ri^2);      %Volume of Coil (m)
ra = (Ri + Ro)/2;             %Average Radius of coil (m)
Ncoil = 340;                  %Number of Coils =480
Ndevices = 1;                 %Number of Devices
Lp = Ndevices*Ncoil*2*pi*ra;  %Path length of coil
Rsis = 15;                    %Resistance of Coil (ohms)=10
%%
%set parameters for posititon and height
step=.00005;
```

```
tol = 0.000001;
xplot=-.025:step:.025; hplot=0:step:0.035;
%%
%Calculate flux density along rotor (T)
B=zeros(length(hplot),length(xplot));
Basum = 0;
i=1;
for x = -.025:step:.025;
    j=1;
    for h = 0:step:0.035
         Bg = Bgh*exp(-h/lg);
        if 0 < x && x < Wp
         Ba = Bg*sin(pi*x/Wp);
        elseif Wp < x && x < 2*Wp
            Ba = Bg*sin(pi*x/Wp);
        elseif 2*Wp < x && x < 3*Wp
            Ba = Bg*sin(pi*x/Wp);
        elseif -Wp < x && x < 0;
            Ba = Bg*sin(pi*x/Wp);
        elseif -2*Wp < x && x < -Wp;
            Ba = Bg*sin(pi*x/Wp);
        elseif -3*Wp < x && x < -2*Wp;
            Ba = Bg*sin(pi*x/Wp);
        else
            Ba = 0;
        end
        B(j,i) = Ba;
        %Find index for flux density at specific height
```

```
            if abs(h-0)<tol
                ind0 = j;
            elseif abs(h-.005)<tol
                ind5 = j;
            elseif abs(h-.0100)<tol
                ind10= j;
            elseif abs(h-.0150)<tol
                ind15=j;
            elseif abs(h-.0200)<tol
                ind20=j;
            elseif abs(h-.0250)<tol
                ind25=j;
            elseif abs(h-.0300)<tol
                ind30=j;
            end
            j=j+1;
        end
        i=i+1;
end
Bave=mean(B);
%%
%plot colormap of simulated magnetic field
figure
set(gca,'FontSize',14)
[C,H] = contour(xplot,hplot,B,500);
title('Magnetic Field Strength Above Magnets','FontSize',18);
xlabel('Horizontal Distance Along Magnets (m)','FontSize',18);
ylabel('Vertical Distance Above Magnets (m)','FontSize',18);
```

```
colorbar;
%%
%Create matrices for flux density at specific heights
[B0,I0] = max(B(ind0,:));
[B5,I5] =  max(B(ind5,:));
[B10,I10] =  max(B(ind10,:));
[B15,I15] =  max(B(ind15,:));
[B20,I20] =  max(B(ind20,:));
[B25,I25] =  max(B(ind25,:));
[B30,I30] =  max(B(ind30,:));
Breal = [0.6200,0.167,0.062,0.025,0.0133,0.0124,0.0049];
Bsim = [B0,B5,B10,B15,B20,B25,B30];
%plot simulated and experimental flux density and error
figure
set(gca,'FontSize',14)
h2 = (0.0:.005:0.03);
plot(h2,Breal,'k-',h2,Bsim,'k:.');
title('Comparison of Simulated and Experimental Magnetic Field'...
    ,'FontSize',18);
xlabel('Radial Distance From Magnets (m)','FontSize',18);
ylabel('Magnetic Field Strength (T)','FontSize',18);
legend('Experimental Magnetic Field','Simulated Magnetic Flux');
axis([-.005,.035,-0.1,1.2]);
diff = abs((Bsim-Breal)./Breal)*100;
avediff = mean(diff);
maxdiff = max(diff);
mindiff = min(diff);
text(0.01,0.8,['Average Percent Error =',num2str(avediff)],...
```

```
    'FontSize',14);
text(0.01,0.75,['Maximum Percent Error =',num2str(maxdiff)],...
    'FontSize',14);
text(0.01,0.7,['Minimum Percent Error =',num2str(mindiff)],...
    'FontSize',14);
```

B.4 Experimental Results Comparison

```
%%
clear
close all
clc
%%
%%% Loading the power data from simulink simulation %%%
%%% choose the correct .mat file to load %%%
matrix = load('Results/26g6'); R=3.4;
% matrix = load('Results/30g6'); R=15;
% matrix = load('Results/20g6'); R=0.5;
% matrix = load('Results/double30_2'); R=25.4;
% matrix = load('Results/31g6'); R=19;
%%% end choose the correct .mat file to load %%%
%%
%%% begin loading power data from simulink
simt = matrix.ans(1,:);
simp = matrix.ans(2,:);
l=length(simt);
%%% end loading power data from simulink %%%
%%
%%% begin loading power data from excel %%%
realt = xlsread('Results/26g_193t_2.0hz.xlsx','A500:A3000');
realp = xlsread('Results/26g_193t_2.0hz.xlsx','B500:B3000');
realv = xlsread('Results/26g_193t_2.0hz.xlsx','D500:D3000');
realf = xlsread('Results/26g_193t_2.0hz.xlsx','C500:C3000');
```

```
% realt = xlsread('Results/30g_340t_2.0hz.xlsx','A500:A3000');
% realp = xlsread('Results/30g_340t_2.0hz.xlsx','B500:B3000');
% realv = xlsread('Results/30g_340t_2.0hz.xlsx','D500:D3000');
% realf = xlsread('Results/30g_340t_2.0hz.xlsx','C500:C3000');

% realt = xlsread('Results/20g_60t_2.0hz.xlsx','A500:A3000');
% realp = xlsread('Results/20g_60t_2.0hz.xlsx','B500:B3000');
% realv = xlsread('Results/20g_60t_2.0hz.xlsx','D500:D3000');
% realf = xlsread('Results/20g_60t_2.0hz.xlsx','C500:C3000');

% realt = xlsread('Results/Double30.xlsx','A500:A3000');
% realp = xlsread('Results/Double30.xlsx','B500:B3000');
% realv = xlsread('Results/Double30.xlsx','D500:D3000');
% realf = xlsread('Results/Double30.xlsx','C500:C3000');

% realt = xlsread('Results/30g_480t_2.0hz.xlsx','A500:A2450');
% realp = xlsread('Results/30g_480t_2.0hz.xlsx','B500:B2450');
% realv = xlsread('Results/30g_480t_2.0hz.xlsx','D500:D2450');
% realf = xlsread('Results/30g_480t_2.0hz.xlsx','C500:C2450');
%%% end loading power data from excel %%%
%%
%%% begin calculating RMS power and RMS voltage of the signals
voltsim = sqrt(R*simp);
voltsimsq = voltsim.^2;
vrmssim = sqrt(mean(voltsimsq));
prmssim = vrmssim^2/R;
vsqreal = realv.^2;
vrmsreal = sqrt(mean(vsqreal));
```

```
prmsreal = vrmsreal^2/R;
y = [prmsreal,prmssim];
figure;
set(gca,'FontSize',14)
bar(y);
ylabel('RMS Power(W)','FontSize',16)
%%% end calulating RMS power and RMS voltage of the signals %%%
%%
%%% begin plot both sets of power data on same plot %%%
tol = .005;
sim1 = find(abs(simt-3)<tol);
sim2 = find(abs(simt-5)<tol);
real1 = find(abs(realt-3)<tol);
real2 = find(abs(realt-5)<tol);
real3 = find(abs(realt-4.1)<tol);
real4 = find(abs(realt-5.1)<tol);
figure;
set(gca,'FontSize',14)
plot(simt,simp,'k--',realt,realp,'b-');
legend('Simulated','Experimental','FontSize',16);
xlabel('Time (s)','FontSize',16);
ylabel('Power (W)','FontSize',16);
title('Comparison of Simulated and Experimental Power'...
    ,'FontSize',16);
%%% end plot both sets of power data on same plot %%%
%%
%%% begin find percent difference between peaks and mean %%%
peakdiff = abs(max(simp)-max(realp))/max(realp)*100;
```

```
meandiff = abs(mean(simp)-mean(realp))/mean(realp)*100;
hold on
text(2.2,.0475,['Average Percent Difference = '...
    ,num2str(meandiff)],'FontSize',14);
fprintf(['Percent Difference of Maximums = %g\n\nPercent',...
    'difference of Means = %g \n\n'],peakdiff,meandiff)
%%% end find percent difference between peaks and mean %%%
%%
%%% begin calculate simulated voltage and plot voltages %%%
simv = (simp.*R).^(0.5);
realv2 = abs(realv);
figure
set(gca,'FontSize',14)
plot(simt(sim1(1):sim2(1)),simv(sim1(1):sim2(1)),'k--',...
    realt(real1:real2),realv2(real1:real2),'b-');
ylabel('Voltage (V)','FontSize',16);
xlabel('Time (s)','FontSize',16);
Title(['Positive voltage of Simulated Signal and Experimental',...
    'Data'],'FontSize',16);
legend('Simulated Voltage','Real Voltage','FontSize',16);
%%% end calculate simulated voltage and plot voltages %%%
%%
%%% Begin plotting the simulated and experimental voltage on single
%%% plot   %%%%
figure
plot(simt,voltsim,'k--',realt,abs(realv),'b-');
ylabel('Voltage (V)','FontSize',16);
xlabel('Time (s)','FontSize',16);
```

```
Title('Absolute Value of Experimental and Simulated Voltage'...
    ,'FontSize',16);
legend('Simulated Voltage','Experimental Voltage','FontSize',16);
set(gca,'FontSize',14)
voltmaxreal = max(abs(realv));
voltmaxsim = max(voltsim);
voltmeanreal = mean(abs(realv));
voltmeansim = mean(voltsim);
vmeandiff = abs((voltmeansim - voltmeanreal)/voltmeanreal)*100;
vmaxdiff = abs((voltmaxsim - voltmaxreal)/voltmaxreal)*100;
%%% end plotting simulated and experimental voltage
%%
%%% Begin Calculating Frequency Data %%%
maxf = max(abs(realf));
meanf = mean(abs(realf));
maxfdiff = abs((2-maxf)/maxf)*100;
meanfdiff = abs((2-meanf)/meanf)*100;
%%% End Calculating Frequency Data %%%
%%
%%% Begin displaying power frequency and voltage data %%%
%Power
disp(['max sim power =',num2str(max(simp))])
disp(['ave sim power  =',num2str(mean(simp))])
disp(['max real power =',num2str(max(abs(realp)))])
disp(['ave real power =',num2str(mean(abs(realp)))])
disp(['max power diff =',num2str(peakdiff)])
disp(['ave power diff =',num2str(meandiff)])
disp(' ')
```

```
disp(' ')
%Voltage
disp(['max sim volt =',num2str(voltmaxsim)])
disp(['ave sim volt  =',num2str(voltmeansim)])
disp(['max real volt =',num2str(voltmaxreal)])
disp(['ave real volt =',num2str(voltmeanreal)])
disp(['max volt diff =',num2str(vmaxdiff)])
disp(['ave volt diff =',num2str(vmeandiff)])
disp(' ')
disp(' ')
%frequency
disp(['max sim freq =',num2str(2)])
disp(['ave sim freq  =',num2str(2)])
disp(['max real freq =',num2str(maxf)])
disp(['ave real freq =',num2str(meanf)])
disp(['max freq diff =',num2str(maxfdiff)])
disp(['ave freq diff =',num2str(meanfdiff)])
disp(' ')
disp(' ')
%%% End displaying power frequency and voltage data %%%
```

B.5 Optimization Simulation

```
clear
close all
M = 1.670; %Load Masskg
Y = 0.025; %Amplitudem

%%
%%% Variables to change %%%
CoilWidth = .001:.0002:.012;
CoilHeight = .001:.0002:.01;
CoilGauge = [38 36 34 32 30 28 26 24];
n1 = length(CoilWidth);
n2 = length(CoilHeight);
n3 = length(CoilGauge);
nameNum = 1;

%%
%%% Run Simulations to find optimal power %%%
meanpower = zeros(n1,n2,n3);
open_system('PowerOptimize.mdl');
for i = 1:n1
    for j = 1:n2
        for l = 1:n3
            g = CoilGauge(l);
            cw = CoilWidth(i);
            ch = CoilHeight(j);
            sim('PowerOptimize')
```

```
            power = load(['Test','.mat']);
            meanpower(i,j,l) = mean(power.ans(2,:));
            nameNum = nameNum+1;
        end
    end
end

fprintf('\n\n\n\n The Simulations Are Complete  \n\n\n');
```

B.6 Optimization Analysis

```
clear
close all
%%
%%% Set parameters of optimization %%%
CoilWidth = .001:.0002:.012;
CoilHeight = .001:.0002:.01;
CoilGauge = [33.5 33 32.5 32 31.5 31 30.5];
n1 = length(CoilWidth);
n2 = length(CoilHeight);
n3 = length(CoilGauge);
%%
%%% load optimiztion data %%%
power = load('meanpower.mat');
meanpower = power.meanpower(:,:,:);
[max_val, position] = max(meanpower(:));
[a b c] = ind2sub(size(meanpower), position);
%%
%%% Print the optimum coil geometry %%%
fprintf(['\n\n\nThe Optimum Coil is %d gauge with a %dm coil',...
    'width and %dm\ncoil height. '],CoilGauge(c),CoilWidth(a)...
    ,CoilHeight(b));
fprintf('The average generation of the coil is %d\n\n\n',max_val);
%%
%%% Plot the power generation of optimum wire size
figure
surf(CoilHeight,CoilWidth,meanpower(:,:,c))
```

```
set(gca,'FontSize',18);
xlabel('Coil Height (m)','FontSize',18);
ylabel('Coil Width (m)','FontSize',18);
zlabel('Average Power (W)','FontSize',18);
title('Average Power of Stator Coil (32awg magnet wire)',...
    'FontSize',20);
```